INORGANIC CHEMISTRY
FRONTIERS

CHINESE CHEMICAL SOCIETY
ROYAL SOCIETY OF CHEMISTRY

RESEARCH ARTICLE

View Article Online
View Journal

Cite this: DOI: 10.1039/d6qi00255b

Lactoferrin as an active coordination scaffold for ruthenium(III)

Tetiana Dyrda-Terniuk, *[a] Michalina Ehlert,[a,b] Kacper Roszak, [c]
Grzegorz Trykowski, [d] Kamil Szpotkowski,[e] Łukasz Skowroński,[e]
Oleksandra Pryshchepa,[a] Rudi van Eldik,[b,f] Katarzyna Mizgalska,[g,h] Wayne Guida,[h]
Aleksandra Karolak, [g] Riddhi Sainda,[i] Prafulla K. Jha[i] and Paweł Pomastowski[a,b]

Received 3rd February 2026,
Accepted 15th March 2026

DOI: 10.1039/d6qi00255b

rsc.li/frontiers-inorganic

This study sought to elucidate the molecular principles by which bovine lactoferrin (bLF) governs ruthenium(III) coordination and to assess how protein-guided binding translates into structural and biological effects. The protein was modified using potassium aquapentachlororuthenate(III) ($K_2[RuCl_5(H_2O)]$) as a metal precursor. The obtained LF–Ru systems were comprehensively examined using spectroscopic (spectrofluorimetry, DLS, ATR-FTIR, SRCD), spectrometric (ICP-OES), microscopic (LM, SEM-EDS, TEM-EDS), scattering (SAXS), and electrophoretic (SDS-PAGE) techniques. Antibacterial activity was evaluated for LF and LF–100Ru against Gram-positive (*Enterococcus faecalis*) and Gram-negative (*Escherichia coli*, *Klebsiella pneumoniae*) bacteria. The cellular response to LF–Ru complexes was investigated using murine fibroblast (L929), human hepatocellular carcinoma (HepG2), and human colorectal adenocarcinoma (Caco-2) cell lines. Molecular docking indicated favorable Ru(III) binding in histidine-containing regions related to native metal-binding motifs. Molecular dynamics simulations supported conformational stability upon metal binding, whereas quantum-mechanical calculations on simplified residue models were used only to assess qualitative donor preferences. The adsorption isotherm was better described by the Langmuir model, indicating saturation-like binding of Ru(III) to accessible LF regions at low and moderate loading. At the highest precursor concentrations, BET-style analysis together with TEM observations suggested additional secondary Ru accumulation within the protein matrix. Fluorescence quenching demonstrated strong interactions in the LF–Ru system (K_a = 1.789 × 10^4 M^{-1}). Desorption studies indicated only minor metal release from LF–100Ru after incubation in simulated gastric and intestinal fluids. Importantly, LF–100Ru reduced the viability of HepG2 and Caco-2 cells while showing comparatively low toxicity toward normal L929 fibroblasts under the tested conditions, indicating a differential cellular response.

1. Introduction

Protein–metal interactions play a significant role in biological systems by controlling catalysis, oxygen transport and storage, electron transfer, structural organization of biomolecules, and cellular signaling and regulatory processes.[1] Understanding the mechanisms of molecular interactions in protein–metal systems is of great value for the design and development of promising therapeutic strategies.[2]

Ruthenium (Ru) complexes are recognized by their wide therapeutic spectrum, including antitumor, antibacterial, and antioxidant activities.[3,4] The multiplicity of Ru oxidation states (from −II to +VIII) enables the synthesis of diverse complexes with a broad range of biological interactions and new mechanisms of action, including DNA damage, ROS-mediated apoptosis, and antimetastatic activity.[5] Among them, Ru(II) and Ru(III) coordination compounds are considered the most appli-

---

[a] BioColl Team, Centre for Modern Interdisciplinary Technologies, Institute of Advanced Studies, Nicolaus Copernicus University in Toruń, Wileńska 4, 87-100 Toruń, Poland. E-mail: tetiana.dyrda-terniuk@umk.pl
[b] Department of Inorganic and Coordination Chemistry, Faculty of Chemistry, Nicolaus Copernicus University in Toruń, Gagarina 7, 87-100 Toruń, Poland
[c] Department of Immunology, Faculty of Biological and Veterinary Sciences, Nicolaus Copernicus University in Toruń, Lwowska 1, 87-100 Toruń, Poland
[d] Department of Materials Chemistry, Adsorption and Catalysis, Faculty of Chemistry, Nicolaus Copernicus University in Toruń, Gagarina 7, 87-100 Toruń, Poland
[e] Department of Surface Physicochemistry, Faculty of Chemical Technology and Engineering, Bydgoszcz University of Science and Technology, Profesora Sylwestra Kaliskiego 7, 85-796 Bydgoszcz, Poland
[f] Department of Chemistry and Pharmacy, University of Erlangen-Nuremberg, Nikolaus-Fiebiger 10, 91058 Erlangen, Germany
[g] Department of Machine Learning, Quantitative Science Division, H. Lee Moffitt Cancer Center and Research Institute, 12902 Magnolia Drive, Tampa, FL 33612, USA
[h] Department of Chemistry, University of South Florida, 4202 East Fowler Avenue, Tampa, FL 33620, USA
[i] Department of Physics, Faculty of Science, The Maharaja Sayajirao University of Baroda, Vadodara, Gujarat 390002, India

cable due to them having the highest chemical stability. Lastly, Ru(III) complexes are considered a better alternative to commonly implemented platinum drugs for cancer treatment, which is mainly attributed to their lower toxicity and better drug resistance.[6,7] However, the most promising Ru(III) drug candidates, namely NAMI-A and KP1019, did not achieve the expected efficiency in clinical chemotherapy studies due to severe side effects and limited bioavailability.[8] A series of limitations necessitated the search for safer and at the same time efficient strategies for cancer treatment.

Targeted therapy is a relatively new and advanced approach in cancer therapy that is not as widely implemented as chemotherapy. The key principle of targeted therapy is based on drugs interacting with specific molecular targets (proteins, *e.g.* receptors, enzymes, factors) responsible for the survival and proliferation of cancer cells.[9] Several advantages offered by targeted therapy, such as improved selectivity and better tolerability by the patient, enabled the development of diverse drug-delivery systems. In this case, a series of emerging challenges related to targeting efficiency, stability of delivery systems, and their biocompatibility must be overcome.

In recent decades, bovine lactoferrin (bLF), a member of the transferrin family of proteins, has been recognized as a potential carrier for biologically active substances, *e.g.* metal ions, nanoparticles, fatty acids, nucleic acids, lipopolysaccharides, vitamins, and other proteins.[10,11] Additionally, bLF is known to be a biodegradable, non-toxic, and non-immunogenic protein that shows antibacterial, antivirus, antioxidant, anti-inflammatory and anticancer activities.[12] This diverse spectrum of biological properties makes bLF an attractive candidate for biomedical applications. It is well defined as a large glycoprotein ($M_w \sim$ 77–91 kDa) characterized by a high binding affinity for iron ($K_A \sim 10^{20}$ M^{-1}).[10,13] Therefore, LF naturally acts as an iron carrier, enabling its efficient intestinal absorption through a receptor-mediated endocytosis mechanism.[14]

LF receptors (LFRs) are expressed on the surface of various types of cells, *e.g.* intestinal epithelial cells, hepatocytes, fibroblasts, lymphocytes, neurons, neutrophils, and macrophages.[15] What is important is that the overexpression of LFRs in cancer cells has been reported, suggesting high potential of LF as a drug carrier for targeted anticancer therapy.[16] It is worthwhile noting the ability of ruthenium to mimic iron for binding to transferrin family proteins; thus it might be assumed that Ru uptake occurs in a similar way to that of Fe – by receptor-mediated endocytosis. Previous studies have primarily focused on investigating interactions between Ru(III) complexes and transferrin (TF); however, information regarding the LF–Ru binding mechanism remains limited.[17] It was shown that KP1019 coordinated to the specific iron-binding sites of human apo-transferrin (apo-hTF) in a 2 : 1 molar ratio, whereas at higher molar ratios, it bound non-specifically.[18] Analogously, Levina *et al.* noticed that KP1019 competed for the iron-binding site in holo-TF, which led to disruption interactions between TF and the TF receptor (TFR), resulting in poor metal uptake.[19] In contrast, Wang *et al.* demonstrated that TF-mediated uptake of Ru(III) by human Caucasian promyelocytic leukemia (HL-60) cells was not affected by coordinated Fe(III), as the two metals occupied distinct binding sites.[20] Although LF and TF belong to the same protein family and share about 60% sequence homology, their structural differences are substantial.[21] For instance, iron release from LF occurs approximately 100 times more slowly than from TF; thus its structure shows a higher resistance to proteolytic digestion.[22] Besides, the isoelectric point of LF is considerably higher (approximately 8–9) compared to TF, which is in the range of around 5–6.[23] The protein isoelectric point significantly affects surface charge properties and, consequently, the tendency to engage in electrostatic interactions with other molecules.[24] Thus, the design of LF–Ru complexes will allow for significant improvement of the delivery of Ru(III) complexes through receptor-mediated pathways.[25] Importantly, the design of LF–Ru complexes may provide new insights into both the structural characteristics and biological activity of the functionalized biomolecule.

This study aims to uncover the molecular principles governing Ru(III) coordination within LF and to evaluate how such protein-guided binding translates into structural and biological outcomes. For this purpose, potassium aquapentachlororuthenate(III) ($K_2[RuCl_5(H_2O)]$) was selected as a precursor. In contrast to commonly used Ru(III) precursors such as ruthenium(III) chloride hydrate ($RuCl_3 \cdot xH_2O$), $K_2[RuCl_5(H_2O)]$ is a well-defined coordination complex with enhanced hydrolytic stability in aqueous solution and reduced tendency toward uncontrolled polymerization.[26–28] Consequently, its use for LF modification provides greater control and reproducibility in binding studies and the preparation of LF–Ru complexes. The given Ru(III) complex was not previously recognized by any specific biological properties; however, it is characterized by high solubility in water and compactness, and therefore we assume it may be easily bound within the LF biomolecule. The nature of interactions in the synthesized LF–Ru complexes was analyzed by a number of spectroscopic (fluorescence spectroscopy, ATR-FTIR, DLS), spectrometric (ICP-OES), scattering (SAXS), microscopic (LM, SEM-EDS, TEM-EDS), and electromigration (SDS-PAGE) techniques. The application of a number of computational methods, including molecular docking, molecular dynamics (MD), and density functional theory (DFT), enabled filling the gap with experimental data. The biological activity of the LF–Ru complexes was assessed by testing their antibacterial properties against Gram-negative (*E. coli*, *K. pneumoniae*) and Gram-positive (*E. faecalis*) bacteria. The impact of the LF–Ru complexes on cell viability along with their cytotoxicity was examined on several cell lines, including murine fibroblast (L929), human hepatocellular carcinoma (HepG2), and human colorectal adenocarcinoma (Caco-2).

2. Experimental

2.1. Materials

The bovine lactoferrin (bLF) used for analysis was the same as in the previous study.[29] Potassium aquapentachlororuthenate

(III) ($K_2[RuCl_5(H_2O)]$), glacial acetic acid (CH_3COOH), and sodium acetate (CH_3COONa) were purchased from Sigma Aldrich (St Louis, Missouri, USA).

2.2. Batch isotherm study of Ru(III) binding to LF

The mechanism of LF–Ru binding was analyzed by using a batch sorption approach. In this study, potassium aquapentachlororuthenate(III) was applied as the ruthenium precursor. Appropriate amounts of the Ru(III) complex were dissolved in 0.1 M acetic buffer (pH 4) at the following concentrations: 1.25, 2.5, 5, 10, 25, 50, 75, 100, 150, 250, and 500 mg L^{-1}. Similarly, LF was suspended in acetic buffer (pH 4) at a concentration of 1000 mg L^{-1} and then mixed with the Ru(III) complex solution at a ratio of 1 : 1 (v/v). The Ru-to-protein molar ratios in the respective mixtures were 0.27/1, 0.53/1, 1.07/1, 2.14/1, 5.34/1, 10.68/1, 16.02/1, 21.36/1, 32.04/1, 53.40/1, and 106.79/1 (mol Ru per mol LF). The reaction mixture was incubated for 24 h at 37 °C and 400 rpm using an Eppendorf ThermoMixer (Hamburg, Germany). Afterwards, it was transferred to an Amicon-0.5 centrifugal filter with a 3 kDa molecular weight cut-off (MWCO) and centrifuged at 14 000 rpm for 5 min to separate the formed complex and the unbound metal ions. The collected filtrate was dissolved in 2% nitric acid and then the Ru(III) concentration was determined by ICP-OES.

2.3. Kinetic study of Ru(III) binding to LF

The mechanism of LF–Ru complex formation was further investigated by performing a kinetic binding study. Initially, the LF solution (1000 mg L^{-1}) was mixed with the Ru(III) complex solution at two different concentrations (10 and 100 mg L^{-1}) at a ratio of 1 : 1 (v/v). The mixture was incubated (37 °C; 400 rpm) for different time periods, namely 2, 5, 10, 20, 30, 60, 120, 300, 450, 600, and 1440 min. Unbound Ru(III) was quantified using the same procedure as that described in the previous step.

2.4. Preparation of LF–Ru complexes

Based on the isothermal and kinetic studies, three concentrations of potassium aquapentachlororuthenate(III) (1.25, 100, and 500 mg L^{-1}) were selected for the large-scale synthesis of LF–Ru complexes, designated as LF–1.25Ru, LF–100Ru, and LF–500Ru, respectively. According to the isothermal study, the molar ratios of bound Ru to bLF in the complexes were determined to be 0.10/1, 8.43/1, and 28.85/1 (mol Ru per mol LF), respectively. The synthesis conditions were identical to those described in section 2.2. After 24 h of incubation, the reaction mixture was transferred to Amicon-15 centrifugal filters with a 3 kDa MWCO and centrifuged (6000 rpm, 4 °C, 40 min). The concentrate containing the LF–Ru complex was washed twice with distilled water and subsequently freeze-dried (−54 °C, 0.080 mbar) overnight using a lyophilizer (Labconco, Kansas City, MO, USA) until a dry powder was obtained.

2.5. Study of the fluorescence properties of the LF–Ru complex

2.5.1. 3D spectra measurements. Initially, LF and LF–100Ru were dissolved in deionized water at a concentration of 100 mg L^{-1}. The 3D fluorescence spectra were recorded using a Jasco FP-8300 spectrofluorometer (JASCO, Easton, MD, USA) at specific excitation (200–730 nm) and emission (210–750 nm) ranges. The measurements were performed at an interval of 5 nm and a scan speed of 5000 nm min^{-1}.

2.5.2. Analysis of the quenching mechanism in the LF–Ru system. A series of solutions of the Ru(III) complex with concentrations of 1.25, 2.5, 5, 10, 25, 50, 75, 100, 150, 250, and 500 mg L^{-1} were prepared for the Stern–Volmer experiment. The protein solution (1000 mg L^{-1}) was mixed with the metal complex in a 1 : 1 (v/v) ratio. The specific maximum emission wavelength was used according to the previously recorded 3D spectra of LF (Fig. S1). The changes in fluorescence intensity were analyzed with a Varioskan™ LUX Multimode Microplate Reader (Thermo Fisher Scientific, Waltham, MA, USA) at $\lambda_{ex}/\lambda_{em}$ = 280/330 nm.

2.6. Particle size and zeta potential measurements

The changes in hydrodynamic diameter and zeta potential of the LF–100Ru complex and LF dispersed in different media (distilled water and 0.1 acetic buffer at pH 4) at a concentration of 1000 mg L^{-1} were analyzed using a Malvern Zetasizer Nano ZS (Malvern Instruments, UK). DTS0012 and DTS1070 cuvettes were used for the particle size and zeta potential measurements, respectively. The analyses were performed at 25 °C with an equilibration time of 120 s by using a manual mode of runs.

2.7. Attenuated total reflectance Fourier transform infrared spectroscopy (ATR-FTIR)

The lyophilized samples of bLF, LF–1.25Ru, LF–100Ru, and LF–500Ru were analyzed in the MIR range (3500–900 cm^{-1}) with a resolution of 4 cm^{-1} using an Alpha FTIR spectrometer (Bruker, Billerica, MA, USA) equipped with a diamond crystal. The collected spectra were subjected to baseline correction using the second derivative method (zeroes) followed by normalization using the OriginPro 2024 software (OriginLab Corporation, Northampton, MA, USA). The amide I band (1720–1580 cm^{-1}) was deconvoluted using the second derivative method (to identify hidden peaks) combined with the Savitzky–Golay smoothing derivative method with a polynomial order of 2 and a window of 20 points. The areas of the fitted peaks were calculated using the Gaussian function. The achieved coefficient of determination (R^2) was 0.999 and a chi-square tolerance value of 1×10^{-6} was reached for each sample. The percentage of each secondary structure type was determined as the ratio of the area of the individual fitted peak (assigned to a given secondary structure) to the sum of the areas of all fitted peaks.

2.8. Synchrotron radiation circular dichroism (SRCD) study

Circular dichroism (CD) spectra of protein samples were recorded on the AU-CD beamline of the ASTRID2 synchrotron radiation source at the Department of Physics and Astronomy, Aarhus University, Denmark. The spectra were collected at 25 °C using a Hellma quartz suprasil cuvette type 121.000 with a nominal 0.1 mm path length under a nitrogen atmosphere. The CD spectra were collected every 1 nm with an average of 2 per measurement. The final CD spectra were calculated as the smoothed average of five independently measured and baseline corrected spectra recorded between 178 and 280 nm. The spectra were smoothed using a seven point Savitzy–Golay filter. The protein concentration was determined using the biuret method. The secondary structure content of analyzed proteins was calculated using BestSel.[30]

2.9. Small angle X-ray scattering (SAXS) analysis

SAXS curves were collected at beamline P12 of the Petra III storage ring at DESY (Deutsches Elektronen-Synchrotron) in Hamburg.[31] Protein samples (20 µL) were analyzed either in deionized water or in phosphate buffer, and the corresponding solvent/buffer was used for background subtraction. Before measurement, the samples were centrifuged to remove aggregates. All data were collected at 15 °C with a scattering vector (s) range of 0.0088–5 nm^{-1}, and overlays of the merged data sets were used to detect concentration-dependent scattering in the lowest s region. All SAXS data were processed using the ATSAS package.[32] Integration, scaling and buffer subtraction were performed using the PRIMUS program. The resulting curves were used for all further calculations and reconstructions. Models were calculated using DAMMIF.[33] Structural parameters and theoretical intensities were calculated using CRYSOL.[34] The radius of gyration (R_g), maximum diameter (D_{max}) and pair-distance distribution function $p(r)$ were determined using GNOM.[35]

2.10. Microscopy imaging

2.10.1. Light microscopy (LM) and scanning electron microscopy with energy-dispersive X-ray spectroscopy (SEM-EDS). Small amounts of the dried bLF, LF–1.25Ru, LF–100Ru, and LF–500Ru samples were mounted on carbon adhesive disks (Leit Tabs) and fixed onto SEM specimen stubs. The morphology and elemental composition were examined using an Axio Zoom.V16 light microscope (Carl Zeiss Microscopy GmbH, Jena, Germany) and an EVO 15 scanning electron microscope (Carl Zeiss Microscopy GmbH, Oberkochen, Germany) equipped with a backscattered electron detector (BSE) and a SmartEDS energy dispersive X-ray spectrometer (EDS).

2.10.2. Transmission electron microscopy with energy-dispersive X-ray spectroscopy (TEM-EDS). TEM samples were prepared by dispersing a few milligrams of the material in 99.8% anhydrous ethanol, followed by sonication for 5 s in an ultrasonic bath. Subsequently, a 5 µL aliquot of the resulting suspension was deposited onto a carbon-coated copper grid with holes (Lacey type, Cu 400 mesh, Plano). The solvent was allowed to evaporate under ambient conditions, and the dried material adhering to the grid was subjected to TEM analysis. The prepared samples were analyzed with a Tecnai X-Twin transmission electron microscope (FEI Company, Hillsboro, OR, USA) equipped with a dark field detector (BF), a high-angle annular dark field detector (HAADF), and an Edax RTEM energy dispersive X-ray spectrometer (EDS).

2.11. Desorption study

Primarily, the LF–100Ru complex was dissolved in water to prepare a solution at a concentration of 10 000 mg L^{-1}. Samples were mixed with gastric (pH 1.4) and intestinal fluids (pH 7.25), prepared according to European Pharmacopeia guidelines,[36] at a 1 : 4 ratio (v/v) and then incubated at 37 °C for 1, 2, and 3 h. Afterwards, the reaction mixture was transferred to Amicon centrifugal filters (cut-off 3 kDa) and centrifuged for 5 min at 14 000 rpm. The remaining filtrate was appropriately dissolved in 2% HNO_3 and the amount of released Ru(III) ions was analyzed using ICP-OES. In parallel, the LF–100Ru solution (10 000 mg L^{-1}) was mineralized in aqua regia at 80 °C for 3 h to determine the initial concentration of Ru(III) in the complex.

2.12. SDS-PAGE analysis

The electrophoretic separation of LF and the LF–100Ru complex was performed in 4–12% polyacrylamide gel (Thermo Scientific, Waltham, MA, USA) under non-reducing conditions. Non-reducing conditions were achieved by adding 5 µL of 4× Bolt lithium dodecyl sulfate (LDS) Sample Buffer (Thermo Scientific, Waltham, MA, USA) to 15 µL of the sample. Electrophoresis was run at 200 V for 22 min using the 1× MES running buffer. Band visualization was performed by gel incubation for 1 h in Coomassie Blue R-350, followed by overnight destaining in deionized water.

2.13. Peptic digestion kinetics

Peptic digestion kinetics were investigated in a similar way to the procedure previously described by Pryshchepa *et al.*[37] Initially, a pepsin stock solution (2000 U mL^{-1}) was prepared in deionized water and subsequently diluted to 5 U mL^{-1} with simulated gastric fluid. The substrates, LF and the 100LF–Ru complex, were individually dissolved in water to obtain working solutions at a concentration of 5000 mg L^{-1}. The enzyme/substrate mixture was prepared at a 0.1 U per 100 µg ratio, in which the final protein concentration was 1000 mg L^{-1}. A series of samples were incubated in an Eppendorf ThermoMixer (Hamburg, Germany) at 37 °C for 1, 2, 5, 15, and 30 min. The reaction was terminated by adding 0.7 M Na_2CO_3 (35% of the total sample volume) to the reaction mixture. Finally, all samples were analyzed by SDS-PAGE in reducing mode. Reducing conditions were achieved by adding 2 µL of 10× Bolt Sample Reducing Agent (Thermo Scientific, Waltham, MA, USA) containing 500 mM dithiothreitol (DTT) per 20 µL of the total reaction mixture.

2.14. Molecular docking in LF–Ru systems

Holo- and apo X-ray crystallography bLF structures were used for docking. In the PDB database, there is only one holo- (iron-saturated) X-ray crystallography bLF with two high affinity metal coordination sites – histidine 253 and 595. This structure (PDB ID: 1BLF) with a resolution of 2.80 Å comprises residues 5–689.[38] Also, there is only one apo- (iron-free) X-ray crystallography structure of bLF (PDB ID: 4OQO), with a resolution of 2.42 Å, which comprises residues 342–689.[39] In this structure, the histidine 253 residue is missing; thus, only the histidine 595 site can be studied. Protein structures were prepared in the Protein Preparation Module of the Schrödinger Suite.[40] Hydrogen atoms were added to the structure, and bond orders and disulfide bonds were assigned. Protein protonation states were assigned using PROPKA at pH 4.0.[41] The protein energy minimization was performed in the OPLS4 force field.[42] The $[RuCl_5(H_2O)]^{2-}$ complex was constructed using Maestro and subjected to DFT geometry optimization and single point energy calculations using Jaguar, an application of the Schrödinger Suite.[43] For geometry optimization, B3LYP-D3 was used with the LANL2DZ basis set for the Ru atom and 6-31G** for the remaining atoms. The calculations were conducted in water solvent using the polarizable continuum model. After geometry optimization, electrostatic potential charges were determined using single point energy calculations, with the total complex charge set to −2. In MetalDock, the ruthenium geometry optimization and single point energy calculations were part of the automated workflow, and were executed using ORCA 5.0.4.[44] DFT calculations utilized the B3LYP theory and the def2-TZVP basis set for all atoms. Molecular docking was performed in the Schrödinger Suite using the Glide application[45] and in the MetalDock[44] workflow, which uses the AutoDock4 docking engine. Two Glide-specific docking methods were used: standard precision and induced fit docking.[46] The docking grid box was centered on the protein histidine residues 253 and 595. MetalDock is an open-source workflow specifically developed for molecular docking of metal complexes to biomolecules. The vacancy in the first coordination sphere of the Ru atom was indicated, and a dummy atom was added to the metal complex for direct coordination of the metal atom to a protein residue. Molecular docking was also performed using AutoDock4 as a docking tool.

2.15. Molecular dynamics (MD) and density functional theory (DFT) studies

We carried out theoretical calculations in two stages: (1) DFT and (2) classical MD. In the DFT calculations, we optimized the structure of individual amino acids, the isolated $[RuCl_5(H_2O)]^{2-}$ complex, and the $[RuCl_5(H_2O)]^{2-}$ complex interacting with amino acids to obtain their minimum-energy ground-state configurations utilizing the Gaussian09 code.[47] The B3LYP hybrid functional was employed, with the GENECP keyword used to define the LANL2DZ basis set for Ru(III), while the 6-31G basis set was applied for Cl, H, O, C, and N atoms.[48,49] The optimized structures and corresponding electron density distributions were visualized using GaussView 5.0. Guided by the molecular docking results, only selected amino acids were considered for quantum mechanical calculations to reduce the computational cost. For each system, all possible binding sites were examined, and the most favorable configuration corresponding to the lowest ground-state energy was chosen for further interaction analysis.

For classical MD simulations, the initial structure of bovine lactoferrin (bLF) was obtained from the RCSB Protein Data Bank: 1BLF for the holo-form and 4OQO for the apo-form. After molecular docking of the three modeled configurations, the highest-scoring pose in each case was used as the starting structure for MD simulations. GROMACS was used for simulations with the CHARMM force field for the protein residues, and EasyPARAM-derived parameters were used for $[RuCl_5]^{2-}$, respectively.[50–52] Before the MD run, the protein with the $[RuCl_5]^{2-}$ complex was solvated with SPC/E water molecules in a cubic box of 10 nm in edge length.[53] The total energy of the system was minimized to relax bonds and remove possible structural clashes. Particle Mesh Ewald (PME) was used to calculate long-range electrostatic interactions, and the cut-off for non-bonded interactions was set to 1.2 nm. After minimization, the system was heated to 300 K under the NVT ensemble using a Langevin thermostat. Subsequently, the system was equilibrated under the NPT ensemble at 1 bar and 310 K. Each equilibration step lasted 100 ps. Production runs were continued for 30 ns, after which the trajectories were analyzed and the root mean square deviation (RMSD) was calculated.

2.16. Resazurin-based assessment of the antibacterial activity of LF and LF–100Ru

The antibacterial response of LF and LF–100Ru was evaluated using three bacterial strains: *Escherichia coli* ATCC 33876, *Enterococcus faecalis* ATCC 51299, and *Klebsiella pneumoniae* B34. Initially, bacteria were inoculated in Mueller–Hinton broth (MHB) and incubated for 24 h under aerobic conditions. Afterwards, the prepared 0.5 McFarland bacterial suspension was diluted 100-fold. A series of solutions of LF and LF–100Ru were prepared in MHB at concentrations of 10 000, 5000, 2500, 1250, 625, and 312.5 mg L^{-1}. Then, 100 μL of bacterial suspension was mixed with 100 μL of the analyzed samples in a 96-well plate and incubated overnight at 37 °C. The bacterial suspension and culture medium alone were used as the positive and negative controls, respectively. Subsequently, 10 μL of resazurin solution (100 mg L^{-1}) was added to each well and the plate was additionally incubated at 37 °C for 1 h. Bacterial viability was determined from the changes in fluorescence intensity at $\lambda_{ex}/\lambda_{em}$ = 560/590 nm using a Varioskan™ LUX Multimode Microplate Reader. All analyses were performed in triplicate for both samples and controls. The value of the negative control was subtracted from each analyzed sample and from the positive control. The fluorescence value of the positive control was taken as 100% bacterial viability.

2.17. *In vitro* cell line assessment

The cytotoxic potential of the LF–Ru complexes was assessed on the L929 murine fibroblast cell line and human epithelial colorectal adenocarcinoma Caco-2 cells, both obtained from the American Type Culture Collection (ATCC), as well as on hepatocellular carcinoma HepG2 cells acquired from the European Collection of Authenticated Cell Cultures (Sigma Aldrich). All cell lines were cultured in high-glucose Dulbecco's modified Eagle's medium (DMEM; Biowest) supplemented with 10% fetal bovine serum (Biological Industries) and antibiotics, namely penicillin (100 U mL^{-1}) and streptomycin (100 μg mL^{-1}) (Capricorn Scientific GmbH). Cultures were incubated at 37 °C in a humidified incubator under a 5% CO_2 atmosphere. Subculturing was performed routinely, 2–3 times a week, using a 0.05% trypsin–EDTA solution (Capricorn Scientific GmbH) once the cells reached approximately 70% confluence.

2.17.1. Cell viability by the MTT assay. The proliferative response of cells to LF–Ru complexes was assessed *via* the MTT assay (3-(4,5-dimethylthiazolyl)-2,5-diphenyltetrazolium bromide; Thermo Fisher Scientific). Initially, L929, HepG2, and Caco-2 cells were seeded into 96-well culture plates (Jet Biofil) at a concentration of 5 × 10^4 cells per mL within 100 μL of supplemented DMEM per well and pre-incubated at 37 °C for 24 h. Following this incubation, cells were exposed to the LF–Ru complexes for 48 h. Stock solutions of the complexes were prepared and then subjected to serial dilutions in the medium to obtain the final concentrations of 625, 1250, 2500 and 5000 mg L^{-1}, respectively. Furthermore, a control sample containing unmodified lactoferrin was prepared, with additional concentrations of 20 000 and 10 000 mg L^{-1}. After treatment, the medium was removed and replaced with 100 μL of MTT solution (0.5 mg mL^{-1}) prepared in PBS. Plates were incubated for 2 h at 37 °C to allow for formazan formation. After the incubation period, the MTT reagent was carefully removed, followed by the addition of 50 μL of absolute dimethyl sulfoxide (DMSO) to each well. The plates were gently agitated for 10 min. Absorbance readings were then taken at 570 nm and a reference wavelength of 630 nm, using a Varioscan™ LUX Multimode Microplate Reader. Viability percentages were calculated by comparing the treated cells to the untreated controls designated as 100% viable. All tests were conducted in five separate replicates. Additionally, observations of cell shape and density were made with an Olympus EP50 inverted phase-contrast microscope.

2.17.2. Measurement of cytotoxic effects through LDH activity. The cytotoxic effects were quantified by measuring lactate dehydrogenase (LDH) release using the CytoTox96 Non-Radioactive Cytotoxicity Assay Kit (Promega, Madison, WI, USA), following the manufacturer's protocol. Each condition was analysed in quintuplicate. For analysis, 50 μL of culture supernatants collected after 48 h of incubation with the test substances from L929 murine fibroblasts, human epithelial colorectal adenocarcinoma Caco-2 cells, and hepatocellular carcinoma HepG2 cells were transferred to a new 96-well plate (Jet Biofil). The CytoTox96 reagent was freshly prepared by combining the assay buffer with the substrate mixture. The positive controls, representing 100% LDH release, were generated by treating cells with 0.8% Triton X-100 for 45 min. The negative controls included untreated cells in the culture medium, while blanks contained the medium alone or the medium with the specified test substance, which were applied in order to eliminate background effects in the measurements. Subsequently, 50 μL of the reagent was added to each well, followed by incubation for 30 min at 21 °C in the dark. The reaction was halted by adding 50 μL of the stop solution. LDH release, reflecting membrane damage, was measured from the absorbance at 490 nm using a Varioskan™ LUX Multimode Microplate Reader. The results are presented as mean values ± standard deviation (SD). Statistical analysis was performed using one-way ANOVA with Tukey's *post hoc* test for multiple comparisons. All computations were carried out using GraphPad Prism 8.0.2 software (La Jolla, CA, USA). The levels of significance are represented as follows: * $p < 0.05$; ** $p < 0.01$; *** $p < 0.001$. For instances where cell viability surpassed the control values of the same concentration of LF, statistical significance was marked with a '#' symbol instead of an asterisk.

3. Results and discussion

3.1. Isotherm study

The binding behavior in the LF–Ru systems was investigated through the application of two isotherm models, namely the Langmuir and Freundlich models (Fig. 1A). A detailed description of the isotherm models and thermodynamic parameters used to analyze Ru(III) binding to LF is provided in the SI.

The calculated sorption parameters for both applied models are shown in Table 1.

The experimental sorption capacity ranged from 0.12 to 36.4 mg g^{-1}. The determined molar ratios of bound Ru to bLF in the formed LF–Ru complexes are shown in Table 2. The q_{eq}/C_{eq} relationship was better fitted by the Langmuir model (R^2 = 0.993) than by the Freundlich model (R^2 = 0.969), indicating a saturation-like binding of Ru(III) to a limited number of accessible LF regions under the studied conditions.[54] The calculated maximum sorption capacity (q_{max}) was 56.9 mg g^{-1}, confirming a substantial affinity of Ru species for LF. The previously determined q_{max} of Fe(III) for LF was 36.3 mg g^{-1}.[55]

Remarkably, R_L decreased as C_0 increased, consistent with the used relationship. The determined dimensionless equilibrium parameter (R_L = 0.28–0.99) indicates favorable LF–Ru formation. Although the experimental data were better fitted by the Langmuir model, a Freundlich contribution should not be excluded, suggesting that the system is not perfectly uniform across the entire loading range. The heterogeneity factor ($1/n < 1$) likewise supports favorable binding.[56] To further probe the high-loading behavior, the data were additionally examined using a modified BET-style representation. The resulting plot suggests that, after an initial saturation-like binding regime, a secondary accumulation step may occur at higher Ru precursor concentrations (Fig. 1B). In this context, the BET-type interpretation should be treated as a phenomenological description of high-loading behavior rather than as proof of classical multilayer adsorption on a porous solid. In particular, it may reflect sec-

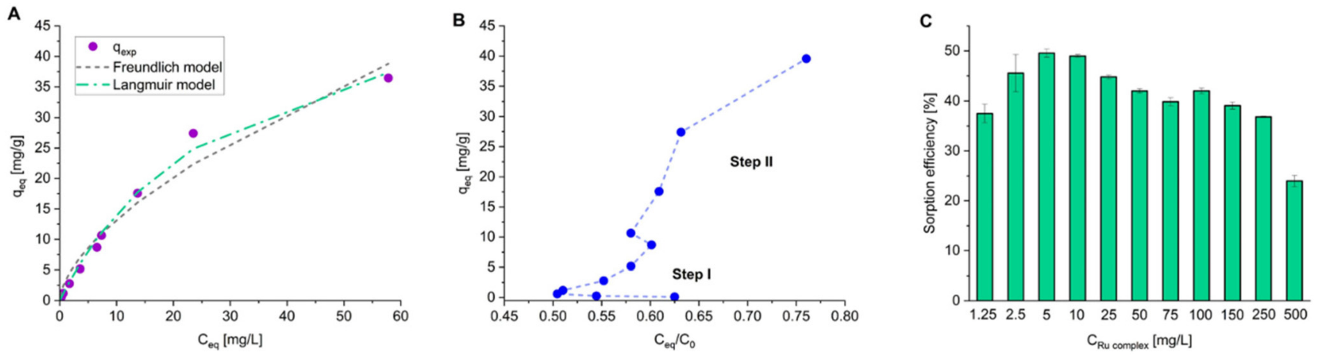

Fig. 1 (A) Isotherm of Ru(III) sorption onto LF, (B) modified BET isotherm, and (C) bar chart of the sorption efficiency of Ru(III) on LF.

Table 1 Sorption parameters for Freundlich and Langmuir models

Freundlich model				Langmuir model			
n	K_F [mg g^{-1}]	S	R^2	q_{max} [mg g^{-1}]	K_L [L mg^{-1}]	S	R^2
1.63	3.24	45.8	0.969	56.9	0.033	10.3	0.993

ondary Ru accumulation or aggregation within the protein matrix instead of a strictly defined surface multilayer. This interpretation is more consistent with the TEM observations obtained for LF–500Ru, where Ru-rich domains were detected only at the highest loading. The calculated binding efficiency of Ru(III) on LF ranged from 24.0 to 49.6% (Fig. 1C). It increased from 37.5 to 49.0–49.6% as the initial Ru(III) complex concentration increased from 1.25 to 10 mg L^{-1}. Subsequently, the efficiency decreased from 44.8 to 24.0% over the 25–500 mg L^{-1} range, supporting progressive saturation of the most accessible binding regions. The calculated change in Gibbs free energy (ΔG) ranged from −19.6 to −16.6 kJ mol^{-1} across the tested concentrations, confirming that LF–Ru formation is spontaneous under the given conditions (T = 310 K). For comparison, the previously determined ΔG values for the LF–Ag system ranged from −25 to −11 kJ mol^{-1}.[37]

3.2. Kinetic study

To evaluate the kinetics of LF–Ru binding, the two initial Ru(III) complex concentrations, namely 10 and 100 mg L^{-1}, were tested (Fig. 2).

A detailed description of the kinetic models used to evaluate Ru(III) binding to LF is provided in the SI. Thus, a zero-order kinetic model was applied to evaluate the changes in Ru(III) concentration over time (C_t). For 10 mg L^{-1} as the initial metal complex concentration, a fast metal binding to LF within 2 min (k_0 = 0.48 mg L^{-1} min^{-1}) was observed, resulting in a decrease of the initial Ru(III) concentration (C_0) from 1.39 mg L^{-1} to a C_t of 0.42 mg L^{-1} (Fig. 2A). In the next step (5–30 min), a gradual increase in C_t from 0.55 to 0.93 mg L^{-1} was observed. This phenomenon might be associated with structural changes in LF, leading to metal desorption and subsequent relocation of Ru(III) to more favorable binding sites. The obtained Weber–Morris plot indicated fast transport of Ru(III) from the solution to the protein surface, which is generally described as boundary layer diffusion and/or external mass transfer (Fig. 2B).[57] Subsequently, a sharp decrease in sorption capacity was observed, which might be caused by the release of weakly bound Ru(III). Finally, the formed LF–Ru system reached equilibrium after 30 min. The calculated sorption efficiency (%E) ranged from 29.2 to 69.7% over the analyzed time period (Fig. 2C). The results are comparable to a zero-order kinetic plot, showing the highest percentage of bound Ru(III) in 2 min, followed by gradual metal desorption and a decrease in sorption efficiency. After 30 min of incubation, the sorption efficiency remained nearly constant (29.2–35.3%), suggesting that the protein had reached its Ru(III)-binding equilibrium, possibly due to saturation of accessible binding sites. In the case of 100 mg L^{-1} as the initial complex concentration, Ru(III) binding to LF was a one-step process which occurred rapidly (k_0 = 3.14 mg L^{-1} min^{-1}) in 2 min (Fig. 2D). A minor desorption of Ru(III) occurred in the range of 2–20 min which corresponded to C_t ~ 9–11 mg L^{-1}. The observed fluctuations might be caused by rearrangements in the LF structure followed by redistribution of the bound Ru(III). The Weber–Morris model confirmed fast binding of metal ions on the external surface (Fig. 2E). It was shown that intra-particle

Table 2 Molar ratios of n(Ru)/n(LF) in the obtained LF–Ru complexes (mol Ru per mol LF)

n(Ru)/n(LF)										
LF–1.25Ru	LF–2.5Ru	LF–5Ru	LF–10Ru	LF–25Ru	LF–50Ru	LF–75Ru	LF–100Ru	LF–150Ru	LF–250Ru	LF–500Ru
0.10/1	0.22/1	0.48/1	0.94/1	2.21/1	4.10/1	6.89/1	8.43/1	13.91/1	21.70/1	28.85/1

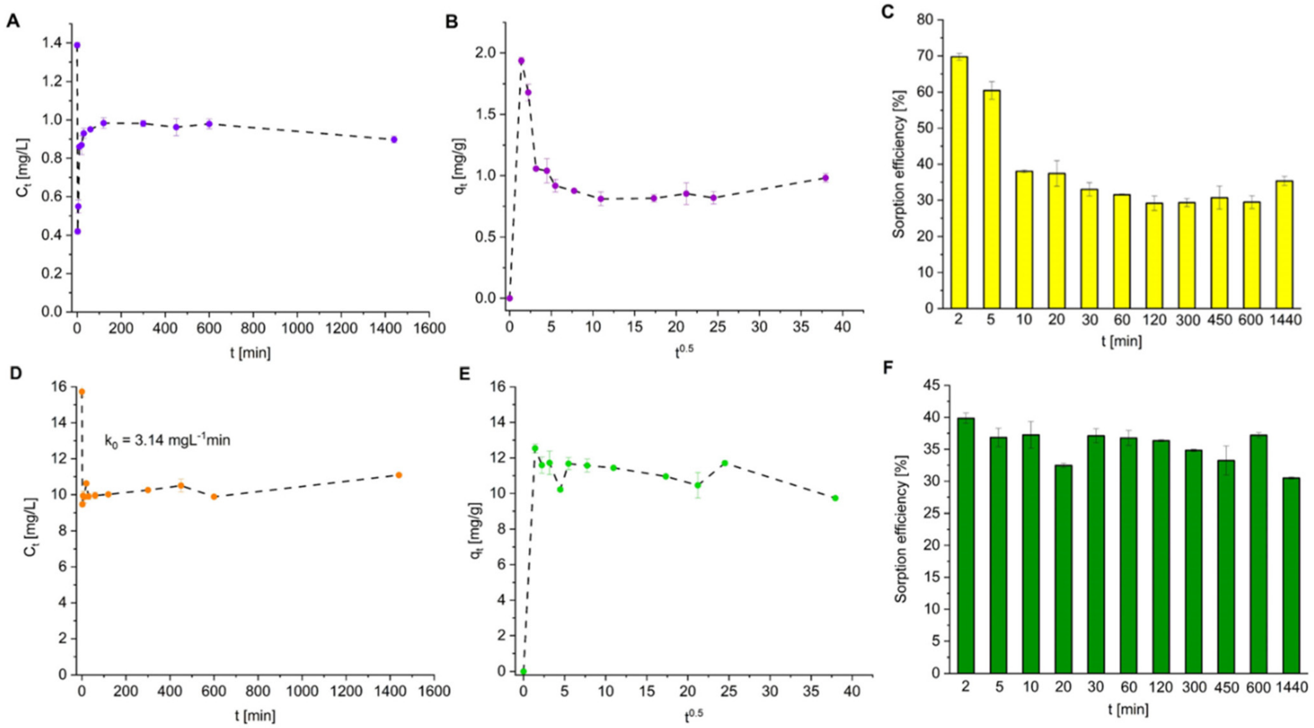

Fig. 2 (A and D) Zero-order kinetic model of LF–Ru binding, (B and E) Weber–Morris intra-particle diffusion model and (C and F) bar chart of the efficiency of Ru(III) sorption onto LF at the applied initial Ru(III) complex concentrations of (A–C) 10 mg L^{-1} and (D–F) 100 mg L^{-1}.

diffusion was not a key rate-limiting step; thus the Ru(III) ions initially bound on the protein surface underwent a brief redistribution before the system reached equilibrium. The calculated sorption efficiency was relatively constant over the whole time period and ranged from 30.5 to 39.9%, indicating greater stability and faster saturation of the LF–Ru complex at a higher initial concentration of the applied complex (Fig. 2F).[58]

3.3. 3D fluorescence spectroscopy analysis

Fig. 3 presents the 3D spectra of LF and the LF–100Ru complex. All registered peaks are labelled in Table 3. Two main peaks at $\lambda_{ex}/\lambda_{em}$ = 280/330 nm and $\lambda_{ex}/\lambda_{em}$ = 225/327 nm are observed in the 3D fluorescence spectra of LF which might be assigned to aromatic amino acids.

The maximum emission peak was slightly blue-shifted from 329 to 328 nm and from 327 to 324 nm after LF–Ru complex formation, which might be explained by less exposure of aromatic amino acid residues, especially Trp, to the polar solvent and rearrangement of their microenvironment to one that is more hydrophobic.[59] Such changes in polarity near Trp could provide more compact and stable protein conformation.[60] The additional peak arising at $\lambda_{ex}/\lambda_{em}$ = 265/531 nm was attributed to the quartz cuvette (Fig. S2). Despite this, the evident fluorescence quenching from 6219 to 3006 a.u. confirms the binding of Ru(III) to bLF. More detailed insights into the nature of the interactions between the fluorophore and quencher were obtained from the Stern–Volmer experiment presented in the next subsection.

3.4. Analysis of the LF–Ru quenching mechanism

The changes in LF fluorescence intensity were examined in a broad range of concentrations of the Ru(III) complex (quencher). Addition of the Ru(III) complex to the LF solution induced an effective decrease in protein fluorescence intensity (Fig. 4A).

Quenching mechanisms were analyzed with the application of the Stern–Volmer eqn (1):

$$F_0/F = 1 + K_{SV}[Q] = 1 + K_q\tau_0[Q] \quad (1)$$

where F and F_0 are the fluorescence intensities of LF with and without the added quencher, K_{SV} is the Stern–Volmer constant (M^{-1}), [Q] is the concentration of the quencher (M), K_q is the quenching rate constant (M^{-1}), and τ_0 is the fluorescence time of the fluorophore without the quencher, which is typically equal to 10^{-8} s.

The evident quenching of fluorescence intensity confirms the binding of Ru(III) to bLF. Based on the Stern–Volmer plot, a linear relationship (R^2 = 0.9895) was observed at low Ru(III) concentrations, up to 0.2 mM, corresponding to a 16 : 1 molar ratio of metal to protein. The determined K_{SV} (Fig. 4B) was (2.044 ± 0.094) × 10^4 M^{-1} in the mentioned concentration range, which indicates a high availability of fluorophores to quencher molecules.[61] For example, the calculated K_{SV} for the system of human transferrin (hTF) and the pentachloro complex of Ru(III) with a bidentate carbazole–pyridine carboxylic acid ligand was equal to 1.09 × 10^5 M^{-1}.[62] As observed, the plot curved upwards at higher metal concentrations. The

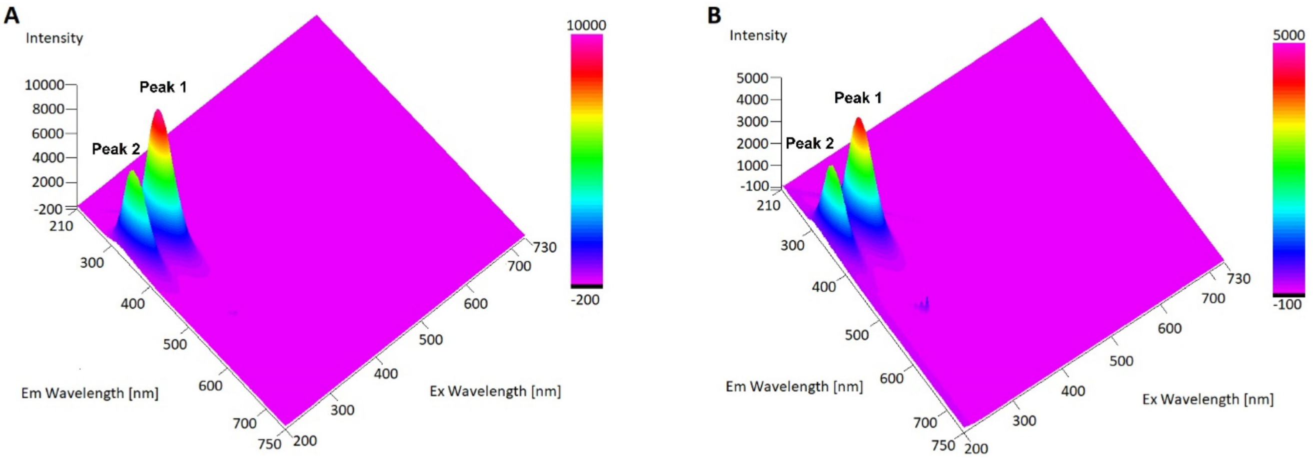

Fig. 3 3D spectra of (A) LF and (B) the LF–100Ru complex dissolved in deionized water at a concentration of 100 mg L^{-1}.

Table 3 Peaks observed on 3D fluorescence spectra of LF and the LF–100Ru complex (100 mg L^{-1})

	Peak 1			Peak 2		
Sample	λ_{ex} [nm]	λ_{em} [nm]	Intensity [a.u.]	λ_{ex} [nm]	λ_{em} [nm]	Intensity [a.u.]
bLF	280	329	9634	225	327	6219
bLF–100Ru	280	328	4397	225	324	3006

positive curvature of the Stern–Volmer plot might be explained by the complicated nature of quenching effects. In general, the fluorescence quenching might be described as either a dynamic mechanism or a static mechanism. Dynamic quenching is characterized by collisional interactions between the biomolecule and quencher molecules in an excited state, while a static mechanism involves the formation of a non-fluorescent ground-state complex.[63] The static quenching phenomenon is commonly observed at high concentrations of the quencher.[64] Thus, we can suggest that the fluorophore–quencher complex forms at $[Q] \geq 0.2$ mM, whereas collision occurs at lower concentrations. Consequently, the obtained plot reflects the combination of both dynamic and static fluorescence quenching mechanisms.[65] Besides, the calculated K_q was equal to 2.044×10^{12} M^{-1} which is much higher than the maximum value of K_q for dynamic quenching. For a more accurate determination of the quenching mechanism, the changes in K_q should be correlated with temperature.[63] Alternatively, the positive curvature might also be associated with the unequal accessibility of fluorophores to the quencher.[66] Indeed, the bLF molecule contains 13 Trp residues, each of which might be differently exposed to the Ru(III) complex.[67]

For a more detailed analysis of the LF–Ru binding mechanism, the double logarithmic eqn (2) was applied and the relevant plot was designed (Fig. 4C):

$$\log[(F_0 - F)/F] = \log K_a + n \log[Q] \qquad (2)$$

where K_a is the binding constant and n is the number of binding sites.

The double log plot of LF–Ru binding showed good linearity ($R^2 = 0.9958$) (Fig. 4D). The calculated K_a was $(1.789 \pm 0.0002) \times 10^4$ M^{-1} and n was 0.998 ± 0.029, indicating strong interactions in the LF–Ru system. Under the tested conditions, this result is best interpreted as one dominant fluorescence-reporting binding event rather than definitive proof that only one Ru-binding site exists in the LF molecule. Similar binding parameters were previously reported for the LF–gallic acid system ($T = 298$ K), where the determined K_a was 1.17×10^4 M^{-1} and n was 1.08.[68] Likewise, Yan *et al.* indicated K_a and n values of $(1.190 \pm 0.012) \times 10^4$ M^{-1} and 1.27 ± 0.02, respectively, for the LF–ginsenoside (LF–Re) system at 298 K.[69] In contrast, the calculated K_a and n values for the apo-hTF/TM34 ruthenium system were $(37.44 \pm 1.27) \times 10^4$ M^{-1} and 1.186, respectively.[70]

3.5. Characterization of the LF and LF–Ru hydrodynamic size and zeta potential changes

DLS results revealed substantial changes in LF size depending on the medium used and the presence of the metal complex (Fig. 5A).

In the case of LF at pH 4, the presence of small particles of 7.5 and 43.8 nm as well as bigger aggregates of 5560 nm was observed; nevertheless, their contribution was much lower in comparison with LF dispersed in water. Remarkably, a notable decrease in the hydrodynamic diameter of LF after binding to the ruthenium complex was observed. The individual sharp peak at 24.3 nm indicates the formation of a monodisperse system. Based on this, ruthenium might be involved in stabilization of the LF structure, preventing protein aggregation. This suggestion was also confirmed by zeta potential measurements.

All analyzed samples displayed a positive zeta potential under the established conditions (Fig. 5B). As expected, LF dispersed in water formed the least stable colloidal system ($\zeta = 9.3 \pm 0.5$ mV), since the pH of the given medium (pH 7) was near the

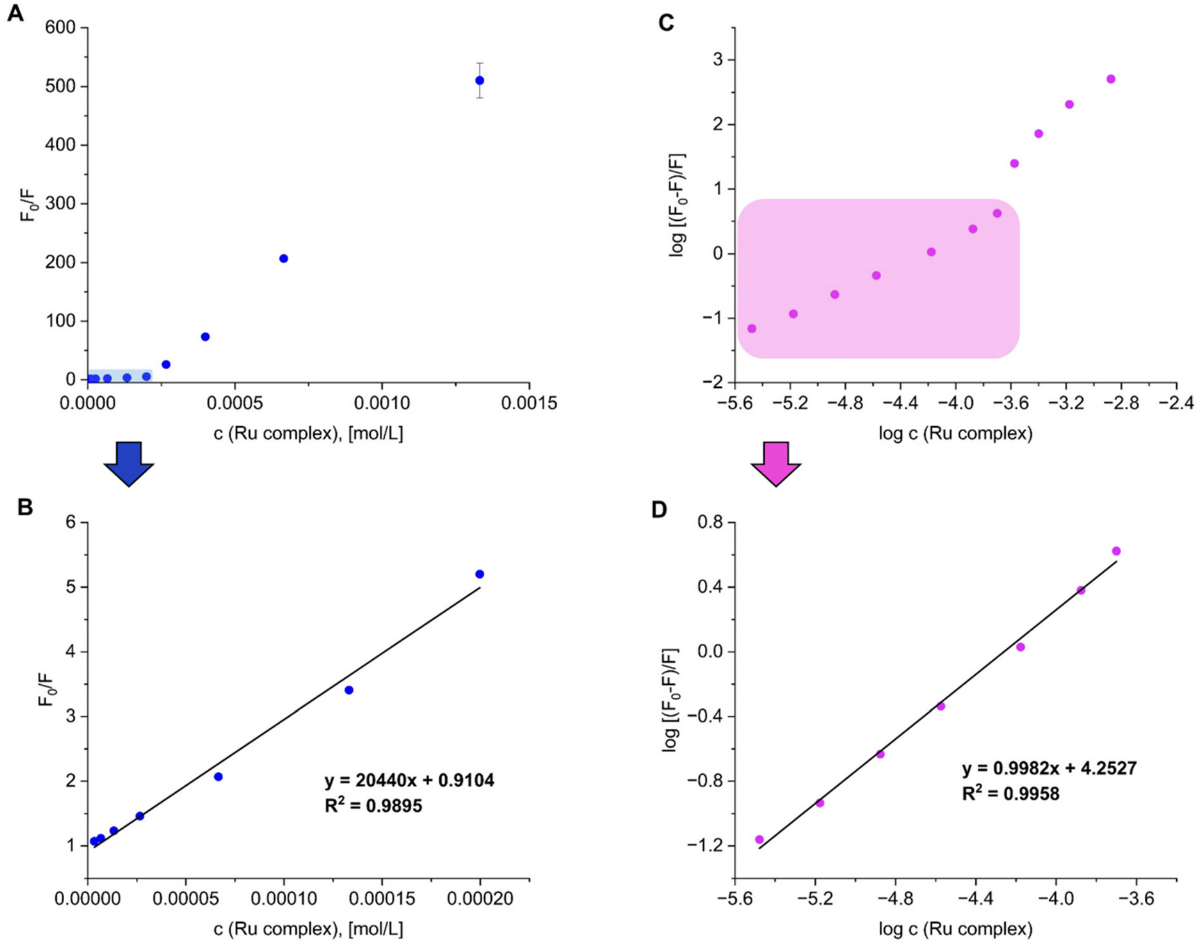

Fig. 4 (A) Stern–Volmer plots for fluorescence quenching in the presence of the ruthenium complex, (B) zoomed-in image of the selected region of Ru(III) complex concentration, (C) double Stern–Volmer plots for fluorescence quenching for the LF–Ru system analyzed at 298 K, and (D) zoomed-in image of the corresponding range of log *c* (Ru complex).

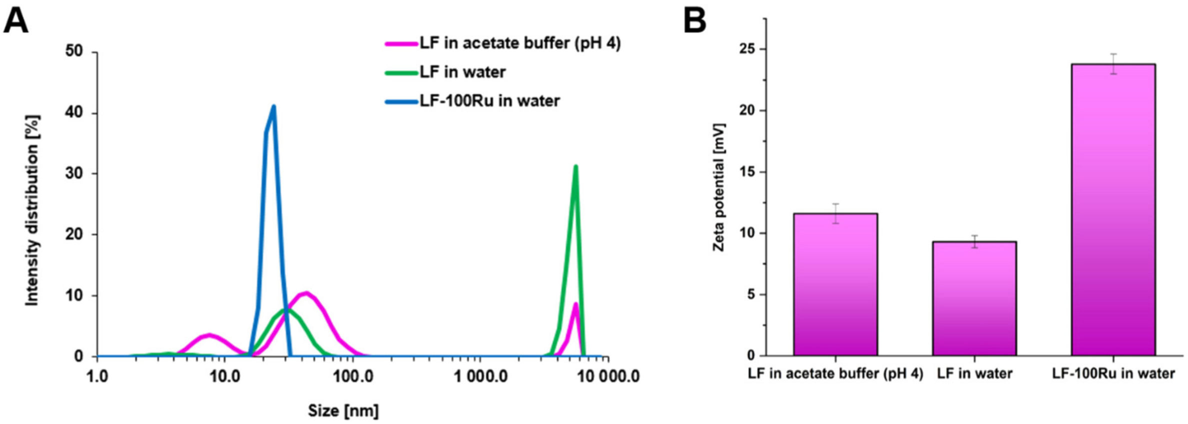

Fig. 5 (A) Particle size distribution and (B) zeta potential of LF and the LF–100Ru complex.

protein isoelectric point (pI). Previously, Pryshchepa *et al.* indicated that the pI of bLF was about 7.4 ± 0.2.[71] In contrast, LF dissolved at pH 4 exhibited a more positively charged surface; thus its zeta potential was $\zeta = 11.6 \pm 0.8$ mV. Similarly, Bokkhim *et al.* showed that the ζ of native LF was +18 at pH 4, and it decreased to +10 mV at pH 7.[72] A more acidic medium typically promotes the protonation of amino ($-NH_2$) functional groups, leading to increased zeta potential.[73] Samples with zeta potentials higher than +20 mV and lower than −20 mV are described as stable.[74] Both LF samples, dispersed in water and in acetic buffer, formed fairly unstable colloids. The addition of the Ru(III) complex significantly affected the LF charge properties. Indeed, LF–Ru showed the highest zeta potential (ζ = 23.8 ± 0.8 mV) among all analyzed samples, thereby forming the most stable colloidal system. The evident increase in zeta potential could be related to conformational changes in the LF structure after Ru(III) binding that led to improved surface availability of positively changed amino acids, such as lysine, arginine, and histidine.[75] Besides, Ru(III) might be potentially involved in interaction with carboxylate groups ($-COO^-$), inducing the neutralization of negative charge in the LF molecule.[73]

3.6. ATR-FTIR

ATR-FTIR analysis was performed to identify the protein functional groups involved in the binding with metal ions. Moreover, the observed shifting of amide bands provided information on the changes in the LF secondary structure. The obtained ATR-FTIR spectra of LF and the respective LF–Ru complexes are shown in Fig. 6.

The characteristic amide A band observed in the range of 3300–3100 cm^{-1} assigned to stretching vibrations of N–H and O–H of the LF functional groups was blue-shifted as the amount of bound Ru(III) in the protein increased.[76] These changes indicate that complexed Ru(III) might affect the strength of hydrogen bonding in the polypeptide backbone. In turn, a peak found at 3100–3050 cm^{-1} was attributed to stretching vibrations of N–H (amide B band). Similar to amide A, it was shifted to a shorter wavelength from 3061 to 3065 cm^{-1}. The characteristic bands observed in the ranges of 2965–2960, 2925–2920, and 2875–2870 cm^{-1} might be attributed to the stretching vibrations of asymmetric $-CH_3$, asymmetric $-CH_2$ and symmetric $-CH_2$, respectively.[77,78]

The range of 1700–1600 cm^{-1} is characteristic of the amide I band and is commonly used for the determination of secondary structure content in the protein since it is considered to be less affected by amino acid side chain vibrations in contrast to amide II and amide III.[79,80] It mainly corresponds to the stretching vibrations of C═O (80%) coupled with the C–N (20%) group in the peptide backbone whose peak position might differ depending on the characteristic secondary structure type, *e.g.* β-sheet (1640–1610 cm^{-1}), random coil (1650–1640 cm^{-1}), α-helix (1660–1650 cm^{-1}), or β-turn (1690–1660 cm^{-1}).[81] Deconvolution of the amide I band allowed us to distinguish the contribution of each type of secondary structure (Fig. 7).

Indeed, β-sheet (50.3%) was the dominant type of secondary structure present in bLF, followed by β-turn (37.3%), α-helix/random coil (11.1%), and aggregated β-sheet (1.3%) (Fig. 8).

A significant increase in α-helix content after Ru(III) complexation indicated that the protein adopted a more stable and ordered conformation, particularly in the LF–100Ru sample, which is consistent with our fluorescence results. A similar tendency was previously observed by Chen *et al.*, resulting in LF complexation with lactose.[82] On the other hand, Alhazmi *et al.* reported that the binding of metal ions, such as Fe(II), Ir(III), and Pt(IV), to BSA caused a visible decrease in α-helix content.[83] It was also indicated that the decrease in α-helix content resulted in AgNP immobilization onto BSA.[84] Interestingly, Hadden *et al.* reported minor differences in the secondary structure of iron unsaturated and saturated hLF.[85] Slight changes in the α-/β-structure ratios observed for LF–1.25Ru and LF–100Ru indicate conformational rearrangements dependent on the amount of bound metal. Besides, loss of α-helix was observed in the LF–500Ru complex simultaneously with the increase of random coil structure. Thus, we can assume that excess bound Ru(III) might negatively affect the stability of the protein, leading to its partial unfolding.

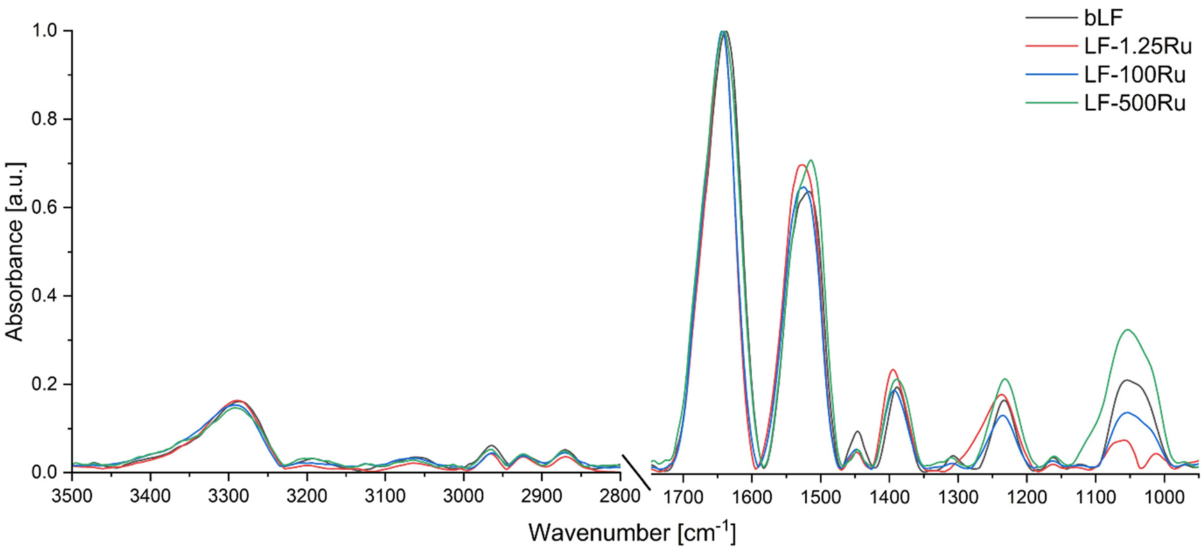

Fig. 6 ATR-FTIR spectra of LF and LF–Ru complexes.

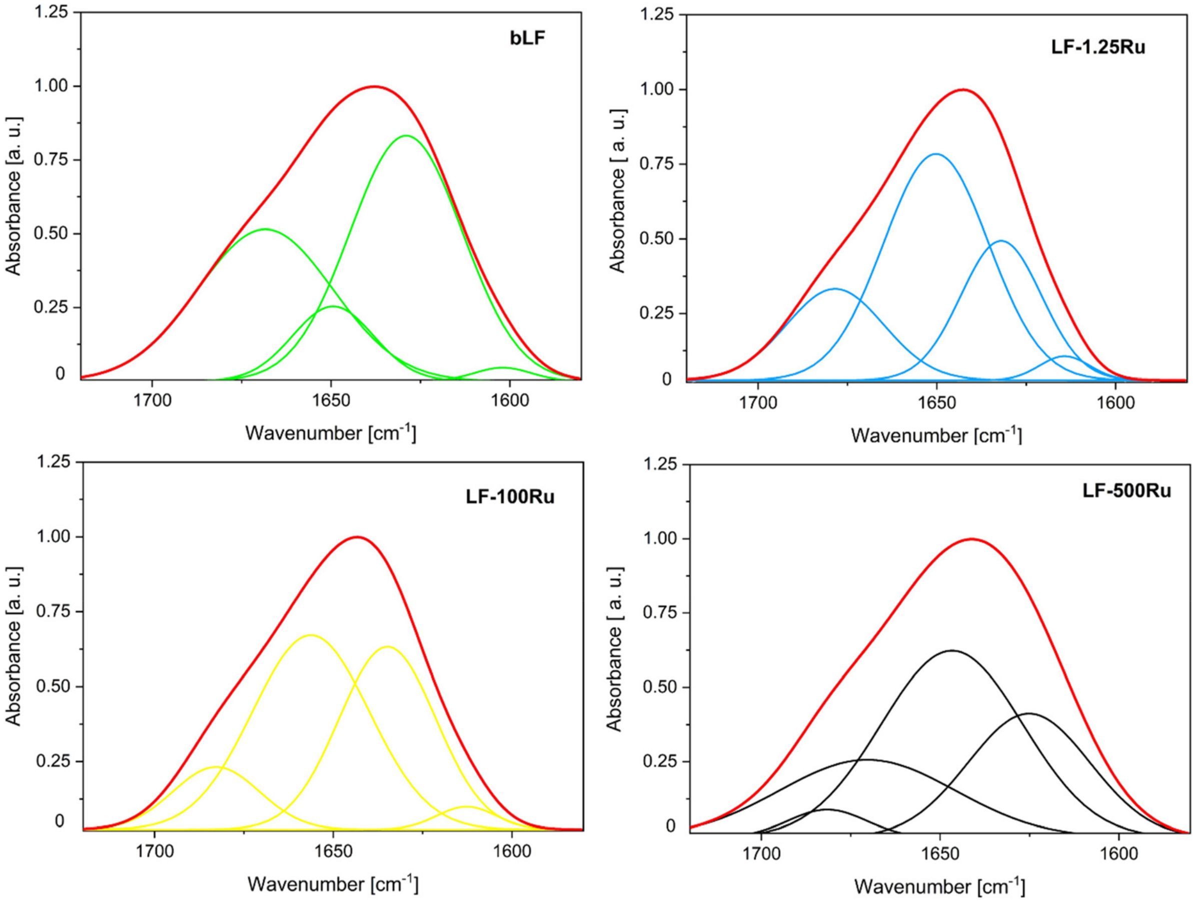

Fig. 7 Amide I band deconvolution results.

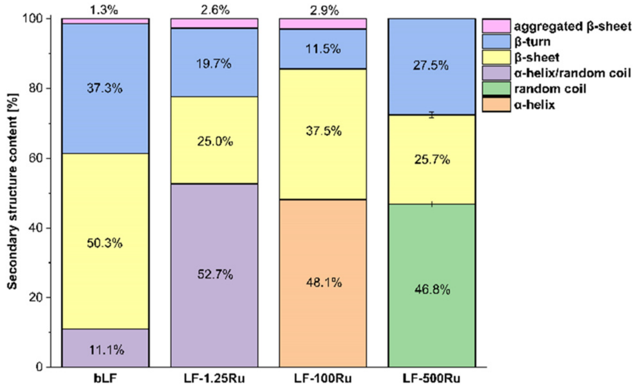

Fig. 8 Changes in the secondary structure composition of LF after its modification with Ru(III).

The amide II band was observed at 1580–1490 cm^{-1} and could be assigned to N–H bending coupled with C–N stretching vibrations.[86] A blue shift from 1517 to 1526 and 1524 cm^{-1} and a red-shift from 1517 to 1515 cm^{-1} were observed in the case of LF–1.25Ru, LF–100Ru, and LF–500Ru, respectively, confirming the conformational changes in the LF induced by binding with the Ru(III) complex. Although the given region is characteristic of a β-sheet structure, it might additionally overlap with the tyrosine C–C ring stretching vibration.[85,87,88] Similarly, peak shifts were observed in the 1240–1230 cm^{-1} and 1165–1160 cm^{-1} ranges, which are also characteristic of the tyrosine side chain.[89] Based on this, we can suggest that tyrosine might be potentially involved in the binding with Ru(III). In turn, the peaks observed at 1450–1440 and 1400–1380 cm^{-1} could arise from the –CH_3 asymmetric and symmetric bending vibrations of the amino acid side chains, respectively.[90] Despite this, the range 1400–1380 cm^{-1} might be attributed to aspartic acid side chain vibrations. Thus, the blue shift of the following absorption band from 1389 to 1395 and 1393 cm^{-1} for LF–1.25Ru and LF–100Ru, respectively, might be a result of the interaction between Ru(III) and the carboxyl group of aspartic acid.[89] The characteristic region of the amide III band is shown at 1350–1200 cm^{-1} which mainly includes N–H bending and C–N stretching vibrations.[91,92] The peaks appearing at 1310–1305 cm^{-1} and 1240–1230 cm^{-1} confirm the presence of α-helix and β-sheet structures, respectively, in LF and LF–Ru samples.[91] In turn, the range 1200–950 cm^{-1} is considered a carbohydrate fingerprint and the appeared peaks might be attributed to the carbohydrate residues (C–O, C–C stretching and C–O–H deformation vibrations) of LF as a glycosylated protein.[78,93,94] The peak

Table 4 Comparison of the secondary structure content between experimental and theoretical data

		Theoretical							Experimental		
Type of secondary structure		1BLF	4OQO	1	2	3	4	5	LF	LF–1.25Ru	LF–100Ru
α-Helix	Helix 1 regular	17.4	17.8	17.4	17.9	17.4	17.4	17.4	16.1	16.7	17.3
	Helix 2 distorted	12.2	12.1	12.2	11.4	12.2	12.2	12.2	0.0	0.0	0.0
Antiparallel β-sheet	Anti 1 left-twisted	0.0	0.0	0.0	0.0	0.0	0.0	0.0	14.1	13.6	11.8
	Anti 2-relaxed	1.7	1.2	1.9	1.9	1.2	1.2	1.7	23.7	25.8	24.3
	Anti 3 right-twisted	10.4	10.7	10.6	9.4	10.6	10.6	10.3	1.6	2.6	1.9
Parallel β-sheet		5.5	6.0	4.9	5.4	5.3	5.3	5.3	0.0	0.0	0.0
β-Turn		18.3	15.6	18.7	17.4	17.5	17.5	17.5	13.3	11.1	12.4
Others (random coil)		34.5	36.6	34.3	36.6	35.8	35.8	35.6	31.3	30.2	32.3

This analysis was performed using the BestSel algorithm, where 1 = glide_His253_holo_1BLF, 2 = glide_His595_apo_4OQO, 3 = glide_His595_holo_1BLF, 4 = metaldock_His253_holo_1BLF, and 5 = metaldock_His595_apo_4OQO.

shifting in the following region after Ru(III) complexation might be caused by the difference in accessibility of glycans resulting in LF conformational changes. Besides, the peak found at 1054 cm^{-1} might be attributed to the tryptophan side chain (C═C or C–N stretching and C–H bending vibrations).[95] As shown, Ru(III) complexation caused shifts in the peak positions, which may be directly associated with conformational modifications in the bLF structure.

3.7. Synchrotron radiation circular dichroism (SRCD)

The following technique was used for studying the changes in bLF secondary structure resulting in Ru(III) binding. The application of the BestSel algorithm allowed for the calculation of secondary structure content from theoretical models. A comparison of the results obtained for the theoretical structures and the experimental data is shown in Table 4 and SRCD spectra are shown in Fig. 9.

The secondary structure element contents calculated for the apo- and holo-forms based on their crystal structures showed only minor differences. Likewise, superposition of the crystal structures indicates that iron ions did not cause significant changes in the spatial organization of bLF (Fig. 10).

In the next step, analysis of the models with docked Ru(III) was carried out. Metal ions did not induce structural changes in the LF structure. As observed, the secondary structure content of the crystallographic and experimental structures of LF showed differences. This might be caused by the high flexibility of LF (random-coil content >30%). On the other hand, the experimental data show that metal complexation does not cause significant changes in the secondary structure of LF with increasing concentrations of Ru(III). This behavior indicates that Ru(III) binds to the LF molecule in a stable manner, without disturbing its secondary structure. As shown, the β-structure was a predominant secondary structure in all analyzed samples with contents ranging from 38 to 42%. The total β-structure percentage for LF–1.25 and LF–100Ru samples was in good agreement with FTIR results; nevertheless, the content of individual structures differed. Remarkably, Ru(III) complexation with LF promoted only a minor increase in α-helix content which is not consistent with previous FTIR results of amide I band deconvolution.

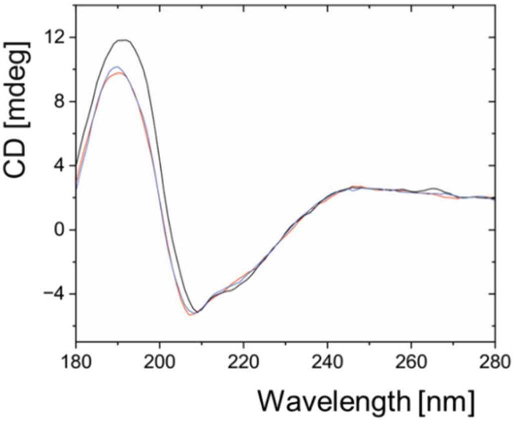

Fig. 9 SRCD spectra of the analyzed samples (black – native LF, red – LF–1.25Ru, blue – LF–100Ru).

The differences in secondary structure content obtained from FTIR and SRCD analyses can be attributed to the specific sensitivities and inherent limitations of each technique. As mentioned previously, CD spectroscopy is considered a more reliable method for quantifying α-helical structures, whereas FTIR spectroscopy is generally more sensitive to β-sheet structures.[96] For example, some amino acid side chains, particularly aspartic acid and glutamic acid, may contribute slightly to peptide bond vibrations in the amide I region (1700–1600 cm^{-1}), potentially affecting FTIR band assignments.[97] On the other hand, a major limitation of CD analysis arises from spectral overlap between peptide backbone signals and contributions from aromatic and sulfur-containing amino acid side chains.[98] Therefore, some authors recommend performing CD measurements at wavelengths below 178 nm to minimize such interference and improve secondary structure discrimination.[99]

3.8. Small angle X-ray scattering

SAXS is a powerful method for studying the structure and oligomerization of proteins in solution and enables calculations

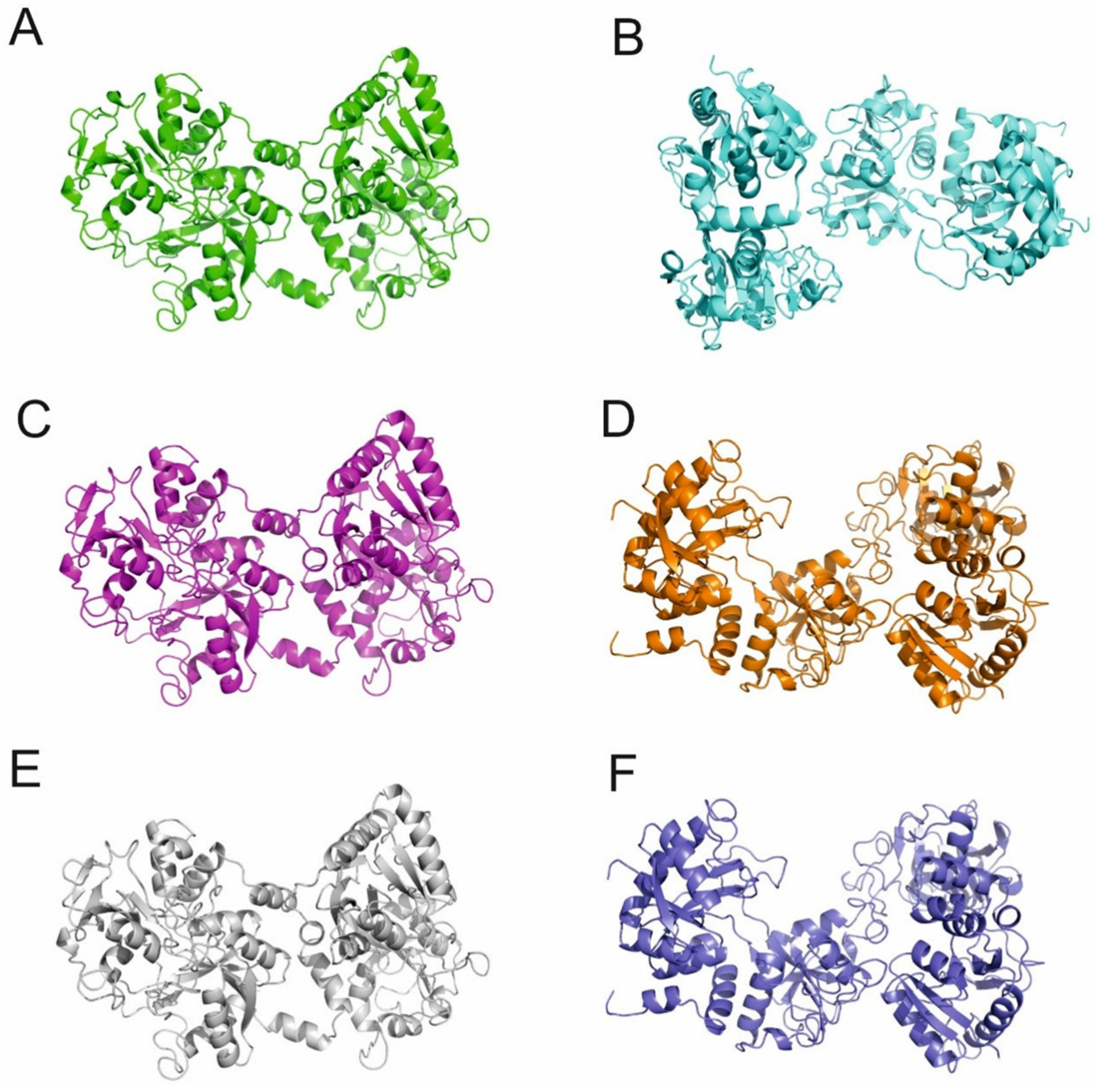

Fig. 10 Comparison of the spatial structures of the analyzed crystal structures and models with docked ruthenium ions (A – 1BLF, B – 4OQO, C – glide_His253_holo_1BLF, D – glide_His595_apo_4OQO, E – metaldock_His253_holo_1BLF, F – metaldock_His595_apo_4OQO).

Table 5 Comparison of structural parameters for crystal structures and analyzed models with docked ruthenium ions, where 1 = glide_His253_holo_1BLF, 2 = glide_His595_apo_4OQO, 3 = glide_His595_holo_1BLF, 4 = metaldock_His253_holo_1BLF, and 5 = metaldock_His595_apo_4OQO

Structural parameters	1BLF	4OQO	1	2	3	4	5
R_g [nm]	3.65	3.68	3.66	3.65	3.65	3.65	3.65
$D_{\max}$ [nm]	9.88	10.3	10.2	9.95	9.96	9.96	9.96
Volume [Å^3]	1.2149×10^5	1.2386×10^5	1.2517×10^5	1.2517×10^5	1.2517×10^5	1.2517×10^5	1.2517×10^5

of structural parameters for crystal structures or theoretical structures. Structural parameters for the analyzed models and experimental data are summarized in Tables 5 and 6, respectively.

The formation of aggregates may be related to changes in the protein surface charge. To assess the influence of the medium, measurements were performed in both water and phosphate buffer. The linearity of the Guinier region confirmed that the analyzed LF solutions were monodisperse under the respective conditions. Based on SAXS data, LF existed predominantly as a dimer in water but as a monomer in phosphate buffer.

The radius of gyration (R_g) of the monomer calculated using CRYSOL is 3.6 nm. The R_g value determined for LF in phosphate buffer was also approximately 3.6 nm, whereas for LF analyzed in water it was about 6 nm. The maximum particle

Table 6 SAXS data collection and structural parameters for LF and LF–Ru complexes

	Sample			
Structural parameters	LF	LF–1.25Ru	LF–100Ru	LF–500Ru
R_g (from $p(r)$) (nm)	5.33	6.06	6.54	5.60
R_g (from Guinier) (nm)	5.17	5.89	6.75	5.78
D_{max} (nm)	17.28	18.18	19.55	19.51

diameter (D_{max}) likewise supported dimerization of LF in water, and the calculated volume led to the same conclusion. Analysis of the pair-distance distribution function and the *ab initio* models indicated an elongated dimer, suggesting association of the monomers along their longitudinal axes. Together, these results show that the ionic strength of the solution strongly influences LF oligomerization: LF behaves predominantly as a monomer in phosphate buffer but as a dimer in water.

Ru(III) interacted with LF and caused measurable changes in its structural parameters. However, only the two lowest precursor concentrations led to an increase in particle size (R_g and D_{max}), whereas the highest concentration decreased the apparent dimer size. This effect is likely related to the higher ionic strength of the solution. Kratky plots provide qualitative information on protein flexibility and unfolding (Fig. 11). The analysis indicates that LF is a highly flexible protein and that Ru(III) modification does not markedly alter the dynamics of the LF polypeptide chain. Within the resolution of the SAXS experiment, ruthenium binding therefore does not appear to disrupt the global LF structure.

3.9. Microscopy study

3.9.1. LM and SEM-EDS. According to the LM images, the LF structure is represented by large irregular plates (Fig. 12A). On the other hand, the surface of LF–Ru complexes became more crushed and granular, resulting in lyophilization (Fig. 12D, G and J). Besides, characteristic changes in the color of the LF–Ru complex with the measurable metal concentration were observed (Fig. 12J). According to the SEM images, the morphology of the LF surface might be described as smooth-plated (Fig. 12B). In turn, the structure of the LF–Ru complexes was characterized by a higher fragmentation degree and increased roughness (Fig. 12E, H and K). The energy-dispersive X-ray spectra indicated carbon (C), nitrogen (N), oxygen (O), and sulfur (S) in all analyzed samples, which are known as key elements that form the protein structure (Fig. 12C, F, I and L). The previously determined weight ratio of C : N : O : S for LF was 54 : 18 : 24 : 1.4, which is consistent with the obtained results.[29] Remarkably, EDS results confirmed an abundance of ruthenium (Ru) element in LF–500Ru (Fig. 12L) samples whose content in the analyzed area was 2.48%. Moreover, the low amounts of iron (Fe), in the range of 0.11–0.18%, observed in all analyzed samples might be explained by the natural ability of LF to chelate Fe(III) ions; thus the initial iron saturation degree was 17% in non-modified LF.[100]

3.9.2. TEM imaging. The obtained TEM images indicated significant changes in the LF microstructure with the increase in bound Ru(III) (Fig. 13). The remarkable increase in C percentage in all samples may be associated with the use of a carbon grid for the analysis. As observed, the LF–1.25Ru sample was mainly characterized by an amorphous protein matrix (Fig. 13A–C). Ruthenium was not detected in the analyzed region, which may be attributed to its low content and to the limited quantitative reliability of EDS in such nanometer-scale regions. The darker domains observed in LF–100Ru may correspond to local Ru-rich regions (Fig. 13E–G). At this stage, these observations should be interpreted cautiously as evidence of heterogeneous Ru accumulation rather than definitive proof of nucleation centers. Analogously to the SEM-EDS results, Ru was detected in LF–500Ru samples (Fig. 13L) at 0.36%. According to the TEM images of LF–500Ru, spherical heterogeneous metal nanoparticles were present (Fig. 13I–K). The particle size ranged from 5 to 10 nm. Lattice fringes visible in the magnified area were consistent with nanostructured crystalline RuO_2, for which the measured interplanar distance (*d*-spacing) was 3.06 Å. This *d*-spacing is characteristic of rutile-type RuO_2 and corresponds to the (110) plane.[101]

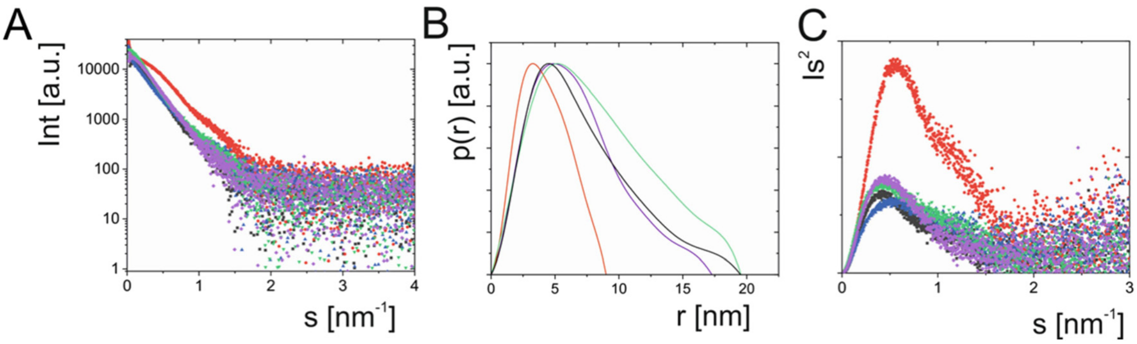

Fig. 11 SAXS data of LF and LF–Ru complexes: (A) experimental X-ray scattering data plotted as a function of the scattering angle for LF, (B) pair-distance distribution function, and (C) Kratky plot for the analyzed samples, where LF – black line, LF in phosphate buffer – red line, LF–1.25Ru – blue line, LF–100Ru – green line, LF–500Ru – violet line.

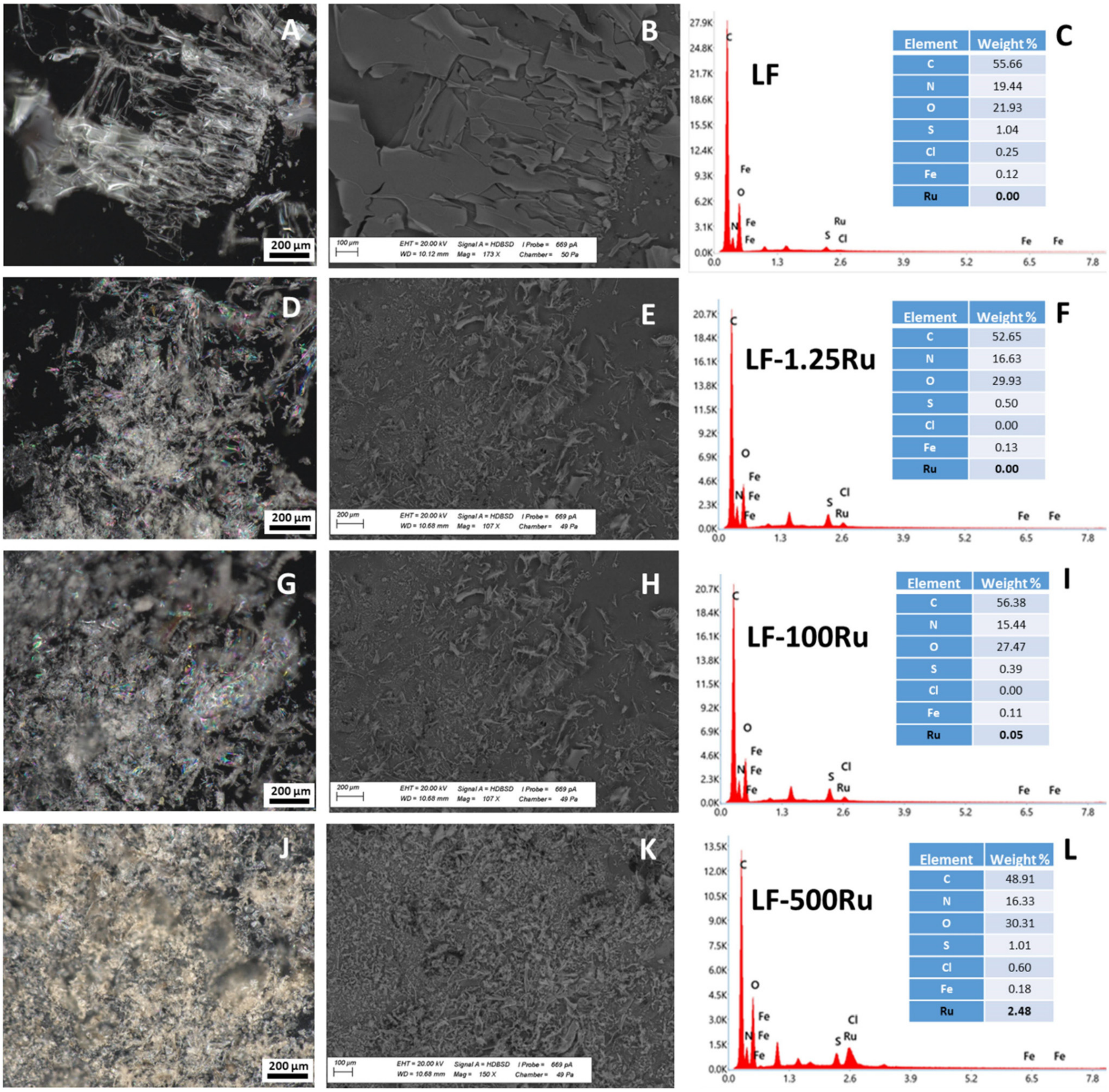

Element	Weight % (C: LF)
C	55.66
N	19.44
O	21.93
S	1.04
Cl	0.25
Fe	0.12
Ru	**0.00**

Element	Weight % (F: LF-1.25Ru)
C	52.65
N	16.63
O	29.93
S	0.50
Cl	0.00
Fe	0.13
Ru	**0.00**

Element	Weight % (I: LF-100Ru)
C	56.38
N	15.44
O	27.47
S	0.39
Cl	0.00
Fe	0.11
Ru	**0.05**

Element	Weight % (L: LF-500Ru)
C	48.91
N	16.33
O	30.31
S	1.01
Cl	0.60
Fe	0.18
Ru	**2.48**

Fig. 12 Images of (A, D, G and J) LM, (B, E, H and K) SEM, and (C, F, I and L) EDS spectra recorded for (A–C) LF, (D–F) LF–1.25Ru, (G–I) LF–100Ru, and (J–L) LF–500Ru.

Protein-assisted synthesis of metal nanoparticles is widely recognized as a green synthetic approach. For example, He *et al.* reported BSA-assisted synthesis of RuO_2 nanoparticles with a mean size of about 7 nm,[102] whereas RuO_2 nanoparticles obtained by green synthesis from *Murraya koenigii* leaves were found in the range of 5–12 nm.[103] Interestingly, Kaur *et al.* suggested that arginine, lysine, and tyrosine may participate in electron-transfer processes during metal-ion reduction,[104] and dissolved oxygen can in turn promote oxidation, leading to metal–oxide nanoparticle formation.[105] However, in the present system, TEM evidence for RuO_2-like NPs was obtained only for LF–500Ru, corresponding to the highest Ru loading. Therefore, any link between LF residues, charge-transfer processes, and nanoparticle growth should be treated as a possible high-loading scenario rather than as a general mechanism of LF–Ru complex formation. The present data do not allow us to conclude that nanoparticle formation contributes to the biological response of LF–1.25Ru or LF–100Ru.

3.10. Desorption study

As indicated, no significant Ru release from LF–100Ru was observed under simulated intestinal conditions over 3 h,

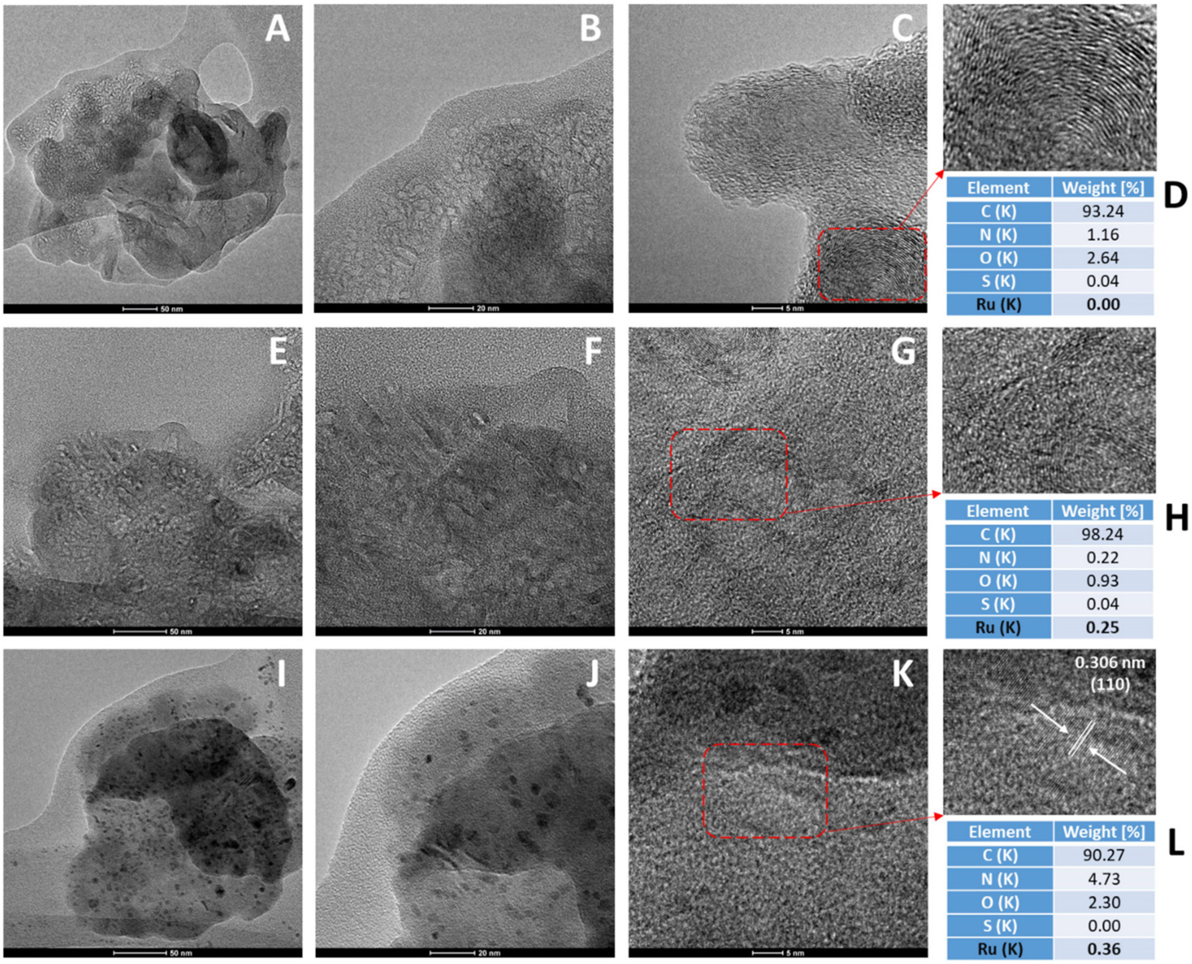

D

Element	Weight [%]
C (K)	93.24
N (K)	1.16
O (K)	2.64
S (K)	0.04
Ru (K)	0.00

H

Element	Weight [%]
C (K)	98.24
N (K)	0.22
O (K)	0.93
S (K)	0.04
Ru (K)	0.25

L

Element	Weight [%]
C (K)	90.27
N (K)	4.73
O (K)	2.30
S (K)	0.00
Ru (K)	0.36

Fig. 13 TEM images of (A–C) LF–1.25Ru, (E–G) LF–100Ru, and (I–K) LF–500Ru and the elemental composition based on EDS results for (D) LF–1.25Ru, (H) LF–100Ru, and (L) LF–500Ru.

whereas metal loss under simulated gastric conditions without enzymes did not exceed 1.5% over the same time. Indeed, Marques *et al.* observed a similar trend in iron release from LF incubated at pH 2 and 7.4 within short time intervals.[95] The evident metal desorption was noticed only after 16 h of incubation at pH 2. Previously, Majka *et al.* confirmed the high sensitivity of LF iron saturation to pH conditions. Thus, the iron content in bLF decreased to about 1% after 24 h of dialysis in citrate buffer at pH 2.[106] Besides, Fe(III) release from bLF incubated in 0.1 M hydrochloric acid (pH 1.2) and phosphate buffer (pH 6.8) for over 2 h accounted for about 58 and 1.1% of the metal, respectively.[55] Based on the desorption study results, a strong binding affinity between bLF and Ru(III) in the formed complex can be assumed, which is consistent with the isotherm and fluorescence study findings. Previously, Raimondi *et al.* related low metal desorption to an effectively irreversible binding process.[57] From a practical perspective, the high stability of LF–100Ru in physiological fluids may positively influence the potential bioavailability of the synthesized complex.

3.11. SDS-PAGE study

SDS-PAGE results indicated a minor difference in electrophoretic mobility between LF and LF–100Ru. The molecular masses of LF and LF–Ru separated under non-reducing conditions were found to be 80 and 77 kDa, respectively (Fig. 14A).

In contrast, the sizes of LF and LF–100Ru were about 90 and 89 kDa under reducing conditions. Previously, a similar phenomenon during the separation of native LF and the LF–Fe complex was noted.[55] The authors related the changes in LF electrophoretic mobility under different modes to the loss of the biomolecule's metal binding properties after the addition of a reducing agent. Additionally, high molecular weight aggregates at $M_w > 150$ kDa were noted in all samples in both reducing and non-reducing modes, which indicated that their association was not regulated *via* disulfide covalent bonds.[107]

The results of pepsin digestion kinetics confirmed a high sensitivity of both samples, LF and the LF complex, to gastric conditions (Fig. 14B). Remarkably, LF–Ru was more stable than LF at the initial stage of digestion (1 min). However, the

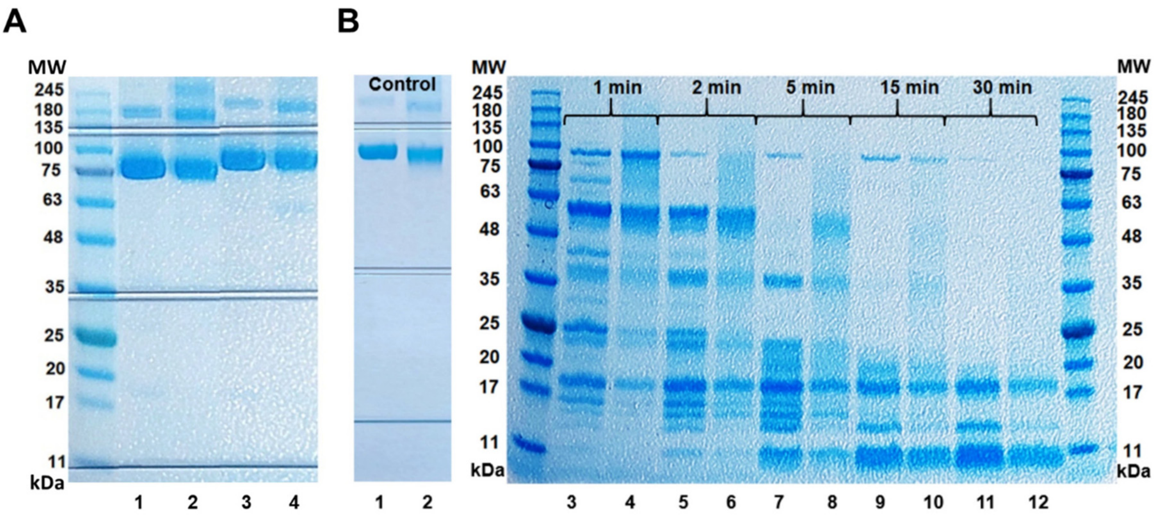

Fig. 14 (A) SDS-PAGE mass profiling of (1, 3) LF and (2, 4) the LF–100Ru complex performed under (1, 2) non-reducing and (3, 4) reducing conditions; (B) pepsin digestion kinetics of (3, 5, 7, 9, and 11) LF and (4, 6, 8, 10, and 12) the LF–100Ru complex performed after 1, 2, 5, 15, and 30 min of substrate incubation with the enzyme; control samples of (1) LF and (2) LF–100Ru.

LF structure showed a higher resistance to pepsin in the later stages (2–30 min). Previously, Pryshchepa *et al.* observed the complete digestion of LF and the LF–Ag complex after 30 min of sample incubation with the enzyme.[37] Taking into account the results of the control digestion, the LF–Ru structure exhibits significantly greater sensitivity to SGF containing pepsin than to SGF alone. Although the desorption study results confirmed a strong binding affinity in the formed LF–Ru complexes, the high digestibility of LF–Ru under gastric conditions minimizes its delivery efficiency to the target place (intestine). Numerous previous studies have demonstrated the potential of protein hydrolysates to act as carriers for various metal ions, including Fe(II), Ca(II), and Zn(II), resulting in enhanced bioaccessibility and bioavailability.[108] The binding affinity of a particular peptide for a metal is mainly influenced by its amino acid sequence, molecular mass, and steric effects.[108] Regarding Ru(III), several amino acids, including histidine (His), cysteine (Cys), lysine (Lys), aspartic acid (Asp), and glutamic acid (Glu), were mentioned as the most significant ligands.[109,110] Despite this, other residues, *e.g.* tyrosine (Tyr), phenylalanine (Phe), glycine (Gly), alanine (Ala), and leucine (Leu) residues, might be successfully involved in the binding of Ru(III). Thus, it can be assumed that efficient peptic digestion does not necessarily result in metal release, as Ru(III) may remain coordinated to peptide fragments generated during digestion. Conversely, the loss of the LF primary structure during proteolysis may impair recognition by specific cellular receptors, potentially reducing metal uptake.[111] To preserve the integrity of the LF–Ru system and facilitate its controlled, site-specific release in the intestine, the application of an appropriate encapsulation approach may be required. Previously, Kilic *et al.* tested bovine serum albumin–tannic acid (BSA-TA) microcapsules in order to enhance the LF bioavailability.[112] The proposed delivery system effectively protected LF against gastric degradation, thus enabling protein release in the small intestine. Moreover, Niu *et al.* showed that LF encapsulated in a pectin-based colloidal system retained approximately 47 ± 1.4% of its native structure after 30 min of *in vitro* gastric digestion, demonstrating a significantly higher degree of protection compared to non-encapsulated LF, for which only 7 ± 1.1% of the native structure remained.[113]

3.12. Molecular docking in the LF–Ru complex

3.12.1. Ligand complex – geometry optimization and single-point calculation. Geometry optimization of the $[RuCl_5(H_2O)]^{2-}$ complex performed using the Schrödinger Suite produced Ru–Cl bond lengths ranging from 2.27 to 2.35 Å, consistent with reported experimental values.[114] The electrostatic potential (ESP) atomic charge on the Ru atom was +0.92, and the complex exhibited a near-octahedral geometry with bond angles of 94–96°. For comparison, geometry optimization performed using ORCA within the MetalDock workflow resulted in slightly longer Ru–Cl bond lengths (2.34–2.43 Å) and a lower Ru atomic charge (+0.52), likely due to differences in the applied basis sets. Nevertheless, the complex geometry remained close to octahedral with bond angles ranging from 94 to 98°.

3.12.2. Molecular docking – H253 site (holo-structure, PDB ID: 1BLF). The potential binding of the Ru(III) complex to bLF was investigated using molecular docking. Prior to docking, the coordinated water molecule was removed from the $[RuCl_5(H_2O)]^{2-}$ complex, as it is expected to dissociate in aqueous biological environments. The DFT-optimized $[RuCl_5]^{2-}$ complex was treated as rigid during docking to preserve its geometry (Fig. S3).

Rigid docking using Glide produced a docking score of −8.708 kcal mol^{-1}, with an initial Ru–Nε (His253) distance of 3.76 Å. After local minimization of the histidine residue, this distance decreased to 2.37 Å, indicating the formation of a coordination bond between Ru and His253 (Fig. 15A and B). The chloride ligands formed salt bridges with positively charged residues (K210, K301, R121) and halogen bonds with Y92, Y192, K210, and K301. The Ru center also interacted with D297 and formed π–cation interactions with Y92 and Y192, which are known to coordinate Fe^{3+} in the native complex. The coordination bond preserved an octahedral geometry with angles of 88.5–92.7°. Distance-constrained docking shortened the Ru–N bond to 2.26 Å but significantly worsened the docking score (−2.006 kcal mol^{-1}). Similarly, induced-fit docking produced a less favorable pose (−4.104 kcal mol^{-1}) with a Ru–His distance exceeding 4 Å, indicating that rigid docking provided the most favorable configuration.

To confirm the docking pose, the MetalDock workflow was applied. A comparable orientation was obtained, with an initial Ru–Nε distance of 2.48 Å, which decreased to 2.61 Å after histidine minimization (Fig. 15C and D). The estimated binding free energy was −6.83 kcal mol^{-1}, and the interaction pattern closely resembled the Glide result, although one coordination angle (78.4°) slightly deviated from ideal octahedral geometry.

3.12.3. Molecular docking – H595 site (holo-structure, PDB ID: 1BLF). Docking at the alternative His595 site was also evaluated. This region forms a sterically constrained environment, and most Glide poses positioned the complex 5–7 Å from the Nε atom of His595. The closest pose showed a Ru–Nε distance of 3.24 Å with a docking score of −2.411 kcal mol^{-1}, suggesting that coordination bond formation is unlikely (Fig. 15E and F).

Similarly, MetalDock docking at this site failed to produce a stable coordination geometry, with the Ru atom remaining approximately 4 Å from the His595 Nε atom.

3.12.4. Molecular docking – H595 site (apo-structure, PDB ID: 4OQO). Docking was also performed using the apo-bLF structure. In this case, the solvent-exposed C-lobe provided greater spatial accessibility around His595, facilitating ligand binding. The best Glide pose showed a Ru–Nε distance of 2.6 Å with a docking score of −3.803 kcal mol^{-1} and the coordination bond geometry featured angles close to 90° (Fig. 15G). MetalDock produced an even closer pose with a Ru–Nε distance of 2.46 Å and an estimated binding free energy of −7.02 kcal mol^{-1}. This configuration was additionally stabilized by interactions with nearby residues, including D395 (Fig. 15H).

3.13. Molecular dynamics

Classical MD simulations were performed to elucidate the interaction mechanism between the $[RuCl_5]^{2-}$ complex and three structural configurations of bovine lactoferrin (bLF). The equilibrated structures obtained after 30 ns of production simulation are shown in Fig. 16. The initial configurations for each system were derived from the molecular docking results to ensure realistic starting orientations of the metal complex within or near the protein binding regions. Throughout the simulation, the $[RuCl_5]^{2-}$ complex exhibited a stable association with several amino acid residues of bLF through short-range non-covalent interactions, including hydrogen bonding, halogen contacts, and van der Waals forces. In the apo-bLF

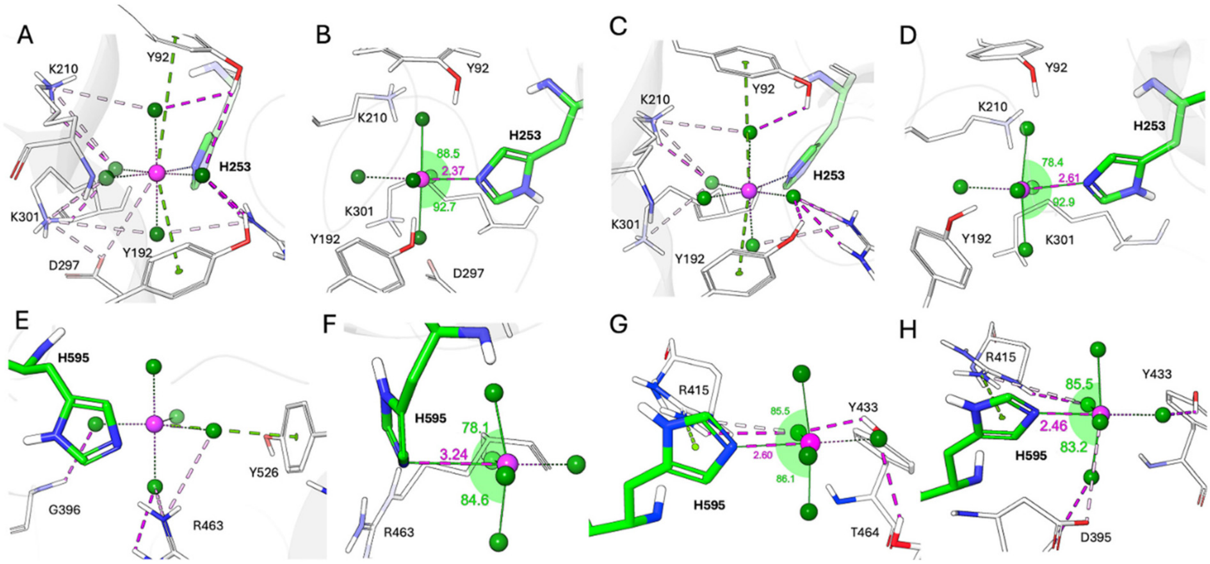

Fig. 15 Molecular docking of the Ru(III) complex to bLF H253 and H595 sites. (A and B) Glide docking to holo-bLF site H253 (PDB ID 1BLF): (A) Ru complex interactions with the residues surrounding the coordination site H253, (B) distance and geometry of the coordination bond to H253 (non-covalent interactions are omitted for clarity); (C and D) MetalDock docking to holo-bLF site H253 (PDB ID 1BLF): (C) Ru complex interactions with the residues surrounding H253, (D) distance and geometry of the coordination bond to H253; (E and F) glide docking to holo-bLF site H595 (PDB ID 1BLF): (E) Ru complex interactions with the residues surrounding the coordination site H595, (F) distance and geometry of the coordination bond to H595; (G and H) docking to apo-bLF site H595 (PDB ID 4OQO): Ru complex interactions and coordination bond obtained using (G) glide and (H) MetalDock. Salt bridges in light pink and halogen bonds in magenta; π–cation interactions in green.

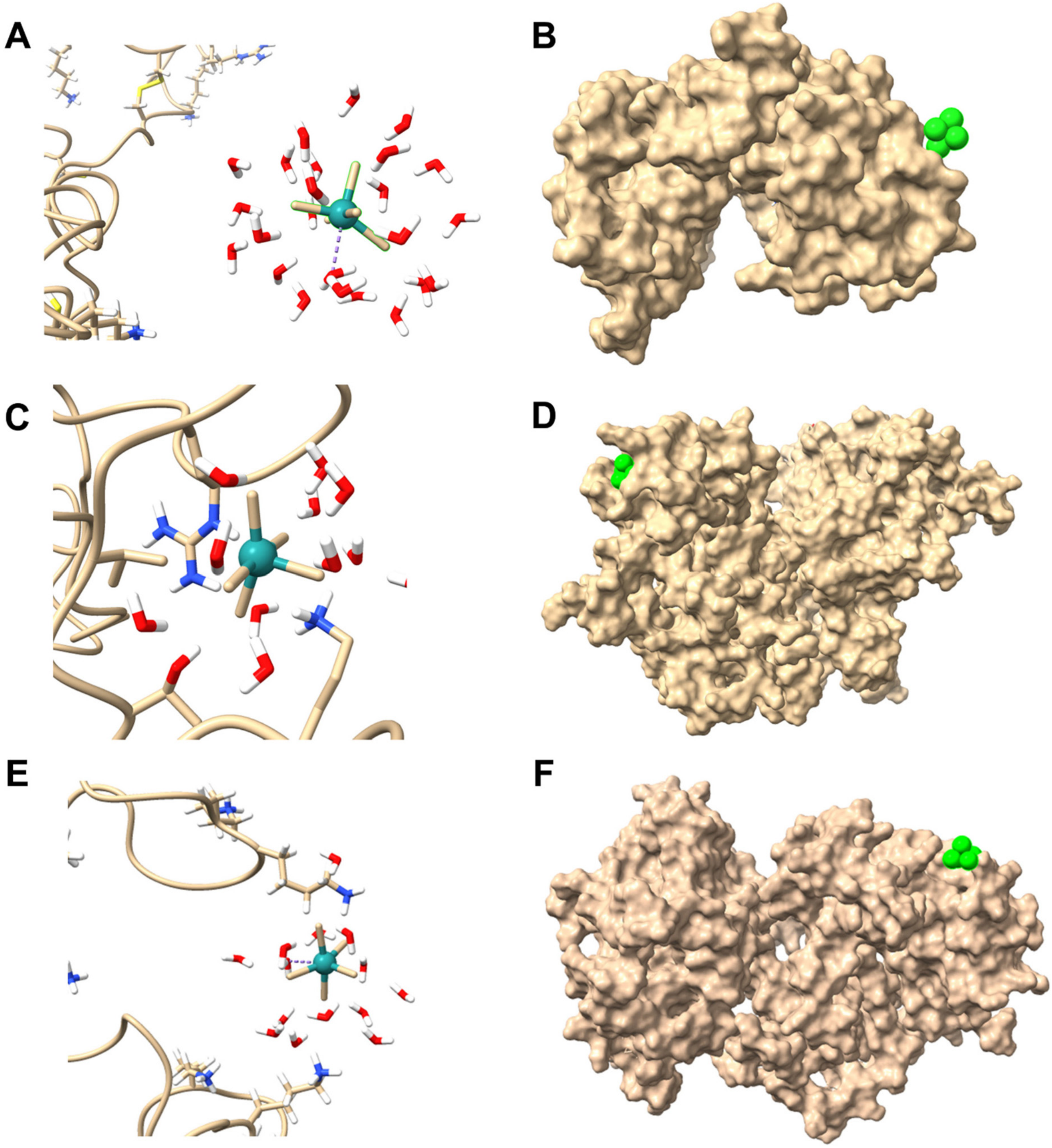

Fig. 16 MD snapshot of BLF with the metal complex after the production run of (A and B) Apo_blf, Holo_blf at His253 (C and D), and His595 (E and F), respectively. The metal complex is shown in (B), (D), and (F) as lime spheres.

system, the complex remained near the protein surface, stabilized by surrounding water molecules that formed a well-defined solvation shell. The closest interaction distances were measured as 3.18 Å between the Ru atom and Cys335 (HB2) and 2.06 Å between Arg349 (HE) and the Cl5 atom of the complex after 28 ns of simulation. By the end of 30 ns, the complex maintained solvation but shifted slightly away from the protein surface, indicating dynamic yet non-dissociative behavior. For the 1BLF–His253 configuration, the metal complex localized near the His253 site, forming comparatively stronger and more stable interactions with several residues: Lys28–HZ2 (2.10 Å), Arg39–HE (2.15 Å), and Thr35–HG1 (2.16 Å). In contrast, in the 1BLF–His595 configuration, the complex stabilized closer to the protein surface with the shortest distances observed for Lys27–HZ2 (1.93 Å) and Lys100–HZ1 (4.53 Å). These observations suggest that arginine and lysine residues play dominant roles in anchoring the complex through short polar contacts, followed by contributions from cysteine and threonine residues. The chlorine atoms of the complex were particularly involved in halogen bonding and

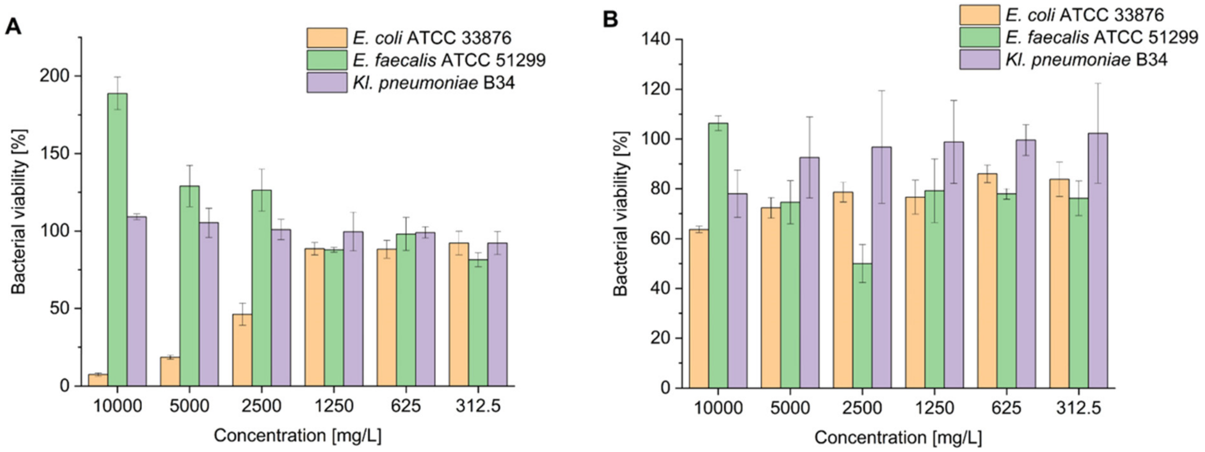

Fig. 17 Changes in bacterial viability ± SD after treatment with (A) LF and (B) the LF–100Ru complex.

weak dispersion interactions with the side-chain donor atoms of these residues. Collectively, these results indicate that both polar and weakly hydrophobic residues cooperatively stabilize the metal complex on the bLF surface, in good agreement with the molecular docking predictions.

The structural stability and conformational behavior of bovine lactoferrin (bLF) upon complexation with the metal complex were evaluated through root mean square deviation (RMSD) analysis, as shown in Fig. S4. RMSD quantifies the average displacement of atomic positions relative to the reference structure and serves as a sensitive indicator of backbone stability and equilibration during molecular dynamics simulations. In all three systems, namely apo-bLF, His253-bound, and His595-bound, an initial rise in RMSD was observed during the first few nanoseconds, corresponding to the relaxation of the protein from its docked conformation toward an energetically favorable state. The apo-bLF configuration showed large fluctuations throughout the simulation, indicating higher conformational flexibility in the absence of the metal complex. In contrast, both holo-systems showed a more gradual RMSD stabilization after approximately 20 ns, reflecting that the protein–metal complex systems had reached equilibrium without any major structural distortion. Among the two holo-configurations, the His253-bound complex maintained the lowest and most stable RMSD plateau suggesting that the coordination of the $[RuCl_5]^{2-}$ anion at this site enhances the rigidity of the surrounding structural domain and promotes overall backbone stability. The equilibrated His595-bound complex exhibited a slightly higher RMSD plateau with moderate fluctuations, implying greater local flexibility near the binding interface. The absence of continuous RMSD drift beyond 20 ns confirms that none of the systems experienced large-scale unfolding or denaturation under the simulated conditions. Collectively, the RMSD profiles demonstrate that the Ru(III) complexation exerts a stabilizing influence on bLF, particularly at the His253 binding site, likely through persistent polar and halogen-mediated interactions that restrict large-amplitude backbone motions. Furthermore, to complement the MD analysis, density functional theory (DFT) calculations were performed on model complexes formed between the $[RuCl_5]^{2-}$ species and representative amino acid functional groups. These calculations are provided in the SI and were designed to study the intrinsic donor preferences of the Ru(III) center toward N-, O-, and S-donor atoms of individual amino acids (Figs. S5 and S6).

3.14. Antibacterial activity of LF and LF–100Ru

The ability of both LF and LF–100Ru to affect the growth of the selected bacterial strains, namely, *E. coli* ATCC 33876, *E. faecalis* ATCC 51299, and *Kl. pneumoniae* B34, was evaluated over a wide concentration range of 312.5–10 000 mg L^{-1} using a resazurin-based assay. This concentration range corresponds to 3.30–105.4 mg L^{-1} of Ru in LF–100Ru. According to the obtained results, both LF and the LF–100Ru complex affected the viability of the analyzed bacterial strains (Fig. 17). It was observed that the viability of *E. coli* notably decreased from 92 to 8% as the protein concentration increased. Previously, Biernbaum *et al.* determined that the MIC values of pure LF and raw LF found in bovine milk for *E. coli* were 3500 and 14 000 mg L^{-1}, respectively.[115] Moreover, it was indicated that LF–Zn and LF–Cu complexes were characterized by higher antibacterial activity against *E. coli* than native and apo-LF.[116,117] The authors assumed that the greater antibacterial potential of metal-modified LF complexes might be associated with their ability to interact with bacterial cell surface, thereby resulting in its damage (bactericidal effect). On the other hand, LF–Mn complexes exhibited moderate antibacterial activity towards *E. coli* and were less effective than native and apo-LF but more effective than holo-LF.[118] The enhanced activity of apo-LF can be attributed to its bacteriostatic mechanism, characterized by iron sequestration and the consequent inhibition of bacterial growth. Based on our results, treatment with LF–100Ru at the highest concentration resulted in a reduction of *E. coli* viability to only 64%. Thus, we can assume that Ru(III) bound to LF may negatively affect the protein's inhibitory activity, either due to the potential occupation of iron-binding sites by the incorporated metal ions or weaker interactions with the bacterial cell membrane. As observed, supplementation with LF promoted the growth of *E. faecalis*; thus, its viability was positively correlated with the protein concentration and increased two-fold at 10 000 mg L^{-1} of LF. In the case of LF–100Ru, the viability of *E. faecalis* ranged from 50 to 107%, depending on the applied complex concentration. Remarkably, the highest inhibitory potential of LF–100Ru was observed at a concentration of 2500 mg L^{-1}. Previously, it was confirmed that *E. faecalis* strains were highly resistant to LF and the protein supplementation may facilitate bacterial growth.[119] Previously, Garbe *et al.* explained this phenomenon with the ability of *E. faecalis* to use glycans found in the LF structure as nutrients.[120] In contrast, Milanowski *et al.* indicated that the MIC value of LF–Ag for *E. faecalis* was 1250 mg L^{-1} which might be associated with the formation of a nanocomplex characterized by a high antibacterial efficiency.[121,122] Previous studies indicated that Ru-based complexes exhibited a much higher antibacterial effect toward Gram-positive species than towards Gram-negative bacteria.[123] For instance, ruthenium incorporation significantly enhanced the antimicrobial activity of shikimate cross-linked chitosan composites against *S. aureus.*[4] Indeed, no significant antibacterial effect of LF was observed against *K. pneumonia*e, whose viability remained relatively constant over the entire concentration range. On the other hand, treatment with LF–100Ru at a concentration of 10 000 mg L^{-1} caused a decrease in bacterial viability to 78%. Remarkably, Murata *et al.* reported that LF at a concentration of 8000 mg L^{-1} inhibited the growth of *K. pneumoniae* by 50%.[124] In contrast, Kutila *et al.* reported that the antimicrobial activity of LF exhibited strain-dependent variability against *K. pneumoniae*.[125] It is worth noting that the tested concentration range primarily allows for the evaluation of biocompatibility and interaction trends rather than therapeutic antibacterial efficacy. For instance, the determined MIC values of eravacycline, the popular synthetic antibiotic, against clinical isolates of *E. coli*, *E. faecalis*, and *K. pneumoniae* were 0.5, 0.25, and 2 mg L^{-1}, respectively.[126] Furthermore, the MIC values of a series of carbene–Ru(II) complexes against *E. coli* ranged from 800 to 1000 mg L^{-1}, whereas the MIC of ampicillin was 3.12 mg L^{-1}.[127] Overall, these findings indicate that Ru(III) coordination modifies the biological response of LF in a strain-dependent manner.

In relation to the obtained digestion results, it is worth noting that LF-derived peptides, including LF1-11, lactoferricin, and lactoferrampin, exhibit strong antibacterial activity and may be more effective against bacteria than intact LF.[128] The reported MIC values for LF and lactoferricin against *Staphylococcus aureus* were 500 and 8 mg L^{-1}, respectively.[124] These N-terminal peptides are highly basic (pI ∼ 9.7–11.7) and interact strongly with negatively charged lipopolysaccharides (LPS), leading to membrane destabilization and subsequent bacterial damage.[128] The desorption study results confirmed the strong binding of Ru(III) to the protein; therefore, it can be assumed that Ru(III) bound to LF fragments may influence their local charge distribution, potentially modulating the strength of peptide–membrane interactions. Despite this, previous structural modelling and MIC studies have demonstrated that the relative positioning of cationic residues flanking the β-strand in lactoferricin, as well as their orientation with respect to hydrophobic tryptophan residues, determines the efficiency of membrane interaction and disruption.[129] On the other hand, Tomita *et al.* reported that the addition of iron (0.1 M $FeSO_4$) had no effect on the antibacterial activity of pepsin-derived LF peptides against *E. coli*, confirming their iron-independent (bactericidal) mechanism of action, in contrast to intact LF.[130,131] In contrast, calcium and magnesium ions at concentrations higher than 0.1 M significantly reduced the activity of lactoferricin by interfering with peptide–membrane interactions.[132] Since the present study does not directly address peptide-level interactions with Ru(III), this aspect remains unclear and could represent an interesting direction for future investigation.

3.15. Cytotoxicity of LF–Ru complexes and their impact on cell viability

To evaluate the effects of the three LF–Ru complexes tested at four different concentrations (625, 1250, 2500 and 5000 mg L^{-1}) on cell viability and membrane integrity, two complementary assays were performed using L929 fibroblasts, HepG2 hepatic cells and Caco-2 intestinal epithelial cells. The MTT and LDH assays were performed to evaluate the biological response of the cells to LF–Ru treatment. The MTT assay (Fig. 18A–C) assesses metabolic activity as an indicator of cell viability, while the LDH assay (Fig. 19A–C) measures membrane integrity, providing complementary information on potential cytotoxic effects. The calculated concentrations of Ru in the respective LF–Ru complexes are shown in Table 7.

For the L929 cell line (Fig. 18A), non-modified LF exhibited cytotoxic effects at 20 000 and 10 000 mg L^{-1}, as evidenced by a significant reduction in cell viability to approximately 50 and 52%, respectively. Therefore, subsequent studies of LF–Ru complexes began at 5000 mg L^{-1}, a concentration at which LF alone showed only borderline cytotoxicity, with viability around 70%. At 2500 mg L^{-1} and below, LF no longer exhibited toxic effects, and a progressive increase in cell proliferation was observed as the concentration decreased. The LF–Ru complexes did not show clear cytotoxicity toward L929 cells under most conditions. However, a decrease in cell viability was observed for LF–100Ru at 625 mg L^{-1} and for LF–1.25Ru at 1250 mg L^{-1}, with viability reaching 72 and 74%, respectively; these results were accompanied by relatively high standard deviations. Notably, at 5000 mg L^{-1}, all three LF–Ru complexes significantly enhanced cell proliferation compared with LF, suggesting that Ru incorporation may reduce the adverse effect of high LF concentrations in this model. The LDH assay results for L929 (Fig. 19A) confirmed the cytotoxicity of high-dose LF, showing a dose-dependent increase in LDH release at 20 000, 10 000, and 5000 mg L^{-1}, indicative of membrane damage and loss of integrity. In contrast, lower LF concentrations (<1250 mg L^{-1}) showed LDH levels comparable to the cellular control. Among the LF–Ru complexes, LF–500Ru

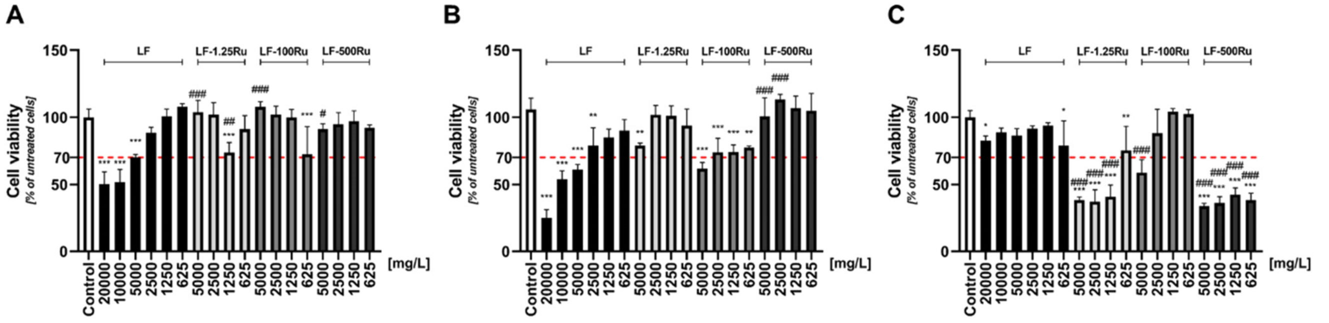

Fig. 18 Viability of (A) L929 fibroblasts, (B) HepG2 cells, and (C) Caco-2 cells following 48 h of incubation with LF, LF–1.25Ru, LF–100Ru, and LF–500Ru was assessed relative to untreated cells (defined as 100%). Results are presented as the mean ± SEM from five independent replicates. Statistical significance is denoted as: * $p < 0.05$, ** $p < 0.01$, *** $p < 0.001$. Comparisons against the LF control are indicated by pound signs (# $p < 0.05$, ## $p < 0.01$, ### $p < 0.001$). A dashed line represents the established cytotoxicity threshold.

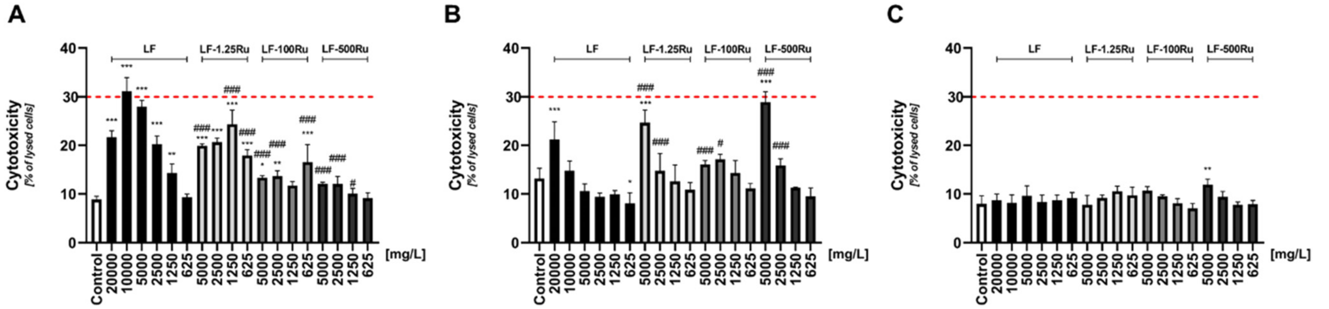

Fig. 19 LDH release from (A) L929 fibroblasts, (B) HepG2 cells, and (C) Caco-2 cells after 48 h of exposure to LF, LF–1.25Ru, LF–100Ru, and LF–500Ru was measured as an indicator of membrane integrity and cytotoxicity, and expressed relative to untreated controls (set as 100%). Data are reported as mean ± SEM from five independent experiments. Statistical significance is indicated as follows: * $p < 0.05$, ** $p < 0.01$, *** $p < 0.001$. Comparisons against the LF-treated group are marked with pound signs (# $p < 0.05$, ## $p < 0.01$, ### $p < 0.001$). The cytotoxicity threshold is denoted by a dashed horizontal line.

Table 7 Ruthenium concentration in the tested LF–Ru complexes

Concentration of the added LF–Ru complex [mg L^{-1}]	LF–1.25Ru		LF–100Ru		LF–500Ru	
	Ruthenium concentration					
	Ru [mg L^{-1}]	Ru [μM]	Ru [mg L^{-1}]	Ru [μM]	Ru [mg L^{-1}]	Ru [μM]
5000	0.62	6.12	52.7	521.2	175.8	1739.6
2500	0.31	3.06	26.3	260.6	87.9	869.8
1250	0.15	1.53	13.2	130.3	44.0	434.9
625	0.08	0.77	6.6	65.2	22.0	217.5

induced only minimal LDH release across all tested concentrations, aligning with the MTT results. Similarly, LF–100Ru displayed low LDH activity (~11–17%). LF–1.25Ru consistently elevated LDH release (~18–25%) across all tested concentrations and therefore showed the highest membrane-damaging tendency among the analyzed formulations, although the overall cytotoxicity remained below 30%.

HepG2 cells (Fig. 18B) exhibited a response to LF similar to that of L929 cells. Concentrations of 20 000, 10 000, and 5000 mg L^{-1} led to a marked decline in viability, to approximately 25, 54, and 61%, respectively. In contrast, LF–500Ru showed a potential stimulatory effect on HepG2 cells at all tested concentrations, with viability at or above 100% and no clear indication of cytotoxicity. While these values did not differ significantly from the cellular control, significant improvements relative to LF-treated cells were observed at 5000 and 2500 mg L^{-1}, suggesting a more favorable response profile. LF–100Ru at 5000 mg L^{-1} showed cytotoxicity comparable to that of LF, with viability around 61%, whereas lower concentrations (625–2500 mg L^{-1}) did not show overt cytotoxicity but remained close to the threshold level. LF–1.25Ru did not display clear cytotoxicity; the 5000 mg L^{-1} dose was borderline, while lower concentrations did not differ significantly from either control. The LDH assay results for HepG2 (Fig. 19B) supported the MTT findings. LF induced a strong, dose-dependent increase in LDH release, with the highest membrane disruption observed at 20 000 mg L^{-1}, reaching approximately 21%. All three LF–Ru complexes showed low LDH levels at 625–1250 mg L^{-1}, consistent with good cellular tolerance. At 5000 mg L^{-1}, elevated LDH activity was recorded for LF–500Ru (~29%), LF–1.25Ru (~25%), and LF–100Ru (~16%). Despite this increase, the MTT data indicated enhanced cell viability in the presence of LF–500Ru and LF–1.25Ru, suggesting that the observed LDH release may reflect transient stress responses rather than classical cytolytic effects.

In Caco-2 cells (Fig. 18C), LF exhibited no cytotoxic activity across the entire concentration range, highlighting its good biocompatibility with intestinal epithelial cells. By contrast, LF–500Ru induced a significant reduction in viability (approximately 34–39%) across all tested concentrations (625–5000 mg L^{-1}), without a clear dose–response trend. LF–100Ru was cytotoxic only at 5000 mg L^{-1}, while lower concentrations were well tolerated. The LF–1.25Ru complex reduced cell viability at concentrations ranging from 5000 to 1250 mg L^{-1}, demonstrating high cytotoxicity (approximately 37–41%). The concentration of 625 mg L^{-1} was considered borderline, with cell viability reaching 75%. Interestingly, LDH measurements in Caco-2 cells (Fig. 19C) revealed low levels of enzyme release across all conditions, regardless of compound or concentration. LDH values remained comparable to the cellular control, indicating preserved membrane integrity and the absence of acute cell damage. This apparent discrepancy with MTT results – where a reduction in metabolic activity was observed, particularly for LF–500Ru – suggests a non-cytolytic mechanism of action. The data indicate that these complexes may exert cytostatic effects, inhibiting proliferation or metabolic function (*e.g.*, *via* cell cycle arrest or mild stress induction), without disrupting membrane structures or inducing necrotic cell death.

The results obtained from the MTT and LDH assays provide important insight into the cellular response to LF and LF–Ru complexes across different models. While LF induced cytotoxic effects in L929 and HepG2 cells at higher concentrations, it did not affect the viability of Caco-2 cells, which is consistent with the known compatibility of LF with intestinal epithelial models. For example, Matsuzaki *et al.* demonstrated that intact bovine LF was actively taken up and released by Caco-2 enterocytes without compromising cell integrity.[133] Zhao *et al.* likewise showed that bLF enhanced Caco-2 viability in a concentration-dependent manner at 50–200 mg L^{-1} and improved transepithelial electrical resistance (TEER) together with tight-junction protein expression.[134] LF–Ru complexes displayed cell-line- and loading-dependent effects rather than a uniform toxicity pattern. LF–500Ru enhanced viability in HepG2 and L929 cells under several conditions, but the same formulation reduced metabolic activity in Caco-2 cells, indicating that its response is context dependent. The most intriguing observations were made in the Caco-2 model, where decreases in metabolic activity occurred together with minimal LDH release. This pattern suggests a predominantly non-cytolytic effect, more consistent with cytostatic or metabolic modulation than with acute membrane damage. In the present study, LF–100Ru was relatively well tolerated by normal L929 fibroblasts, while a decrease in viability was observed for HepG2 and Caco-2 cancer cells at 5000 mg L^{-1} (corresponding to 521.2 μM Ru). These findings indicate a differential cellular response under the tested conditions rather than pharmacological selectivity. For comparison, cisplatin has been reported to induce approximately 90% loss of colorectal cancer cell viability (HT29 and SW480) at 10 μM, whereas KP1019 reduces cell viability by about 50% (IC_{50}) at 50–80 μM, depending on the cell line.[135] Similarly, the IC_{50} values of a series of Ru(II) polypyridyl complexes and cisplatin against HepG2 cells were 17.7–25.3 μM and 11.5 μM, respectively.[136] Notably, the corresponding free ligands did not exhibit cytotoxicity. Such observations highlight that Ru-based systems often exhibit biological effects at comparatively higher concentrations than platinum drugs. In contrast, although NAMI-A demonstrated significant antimetastatic activity, it did not decrease the viability of mammary adenocarcinoma (TS/A), oral carcinoma (KB), or melanoma (B16-F10) cell lines even at 100 μM,[137] and its reported IC_{50} against HT-29 cells was 339 μM.[138] Accordingly, the assays performed in this study were intended primarily to evaluate biocompatibility and preliminary cellular responses rather than therapeutic efficacy.

Cellular morphology was evaluated after 48 h of incubation using an inverted phase-contrast microscope. All images are shown in the SI. Representative images of L929 fibroblasts (Fig. S7), HepG2 hepatocytes (Fig. S8), and Caco-2 epithelial cells (Fig. S9) are presented after exposure to all three LF–Ru complexes at 5000 and 625 mg L^{-1} together with the respective controls.

The comparative analysis of cell morphology was consistent with the results of the MTT and LDH assays, further confirming the observed cytotoxic or biocompatible effects of the tested compounds. Microscopic analysis of L929 fibroblasts revealed a typical spindle-shaped morphology and uniform adherence, consistent with healthy cell architecture. No signs of cytotoxic damage were observed. The LF–500Ru complex was suspended directly in the culture medium, which explains the presence of dark particulate matter visible in all its micrographs.

Phase-contrast microscopy of HepG2 cells revealed morphology consistent with the biochemical assays. In cultures treated with LF–500Ru, both tested concentrations (5000 and 625 mg L^{-1}) preserved normal epithelial features: the cells remained polygonal, tightly packed, and adherent, indicating good cytocompatibility. This was particularly evident at 625 mg L^{-1}, where the image was not disturbed by visible particles of the complex. Treatment with LF–100Ru at 5000 mg L^{-1} led to visible morphological alterations, including cell rounding, partial detachment, and decreased confluence, consistent with cytotoxicity; however, at 625 mg L^{-1}, most cells maintained near-normal morphology. For LF–1.25Ru, cells exposed to 5000 mg L^{-1} showed minor morphological changes, such as reduced density and occasional rounding, whereas at 625 mg L^{-1}, the monolayer structure remained largely intact.

In the control and LF-treated cells at both 5000 and 625 mg L^{-1}, Caco-2 cells maintained a characteristic cobblestone-like morphology and dense monolayer structure, indicative of high viability and the absence of overt cytotoxicity. Microscopic evaluation of Caco-2 cells after treatment with LF–Ru complexes revealed changes that were generally consistent with the viability and LDH results, although not all biochemical effects were mirrored by marked structural damage. Although the

MTT assay showed reduced metabolic activity for LF–Ru complexes at 5000 mg L^{-1}, phase-contrast microscopy revealed only minor morphological changes at both tested concentrations (5000 and 625 mg L^{-1}). The cells displayed reduced density but largely retained their epithelial cobblestone morphology, with only minor signs of reduced confluence and focal detachment. These results suggest that metabolic activity was impaired, as confirmed by the MTT assay, whereas overall membrane integrity and basic cell architecture remained relatively preserved, consistent with the low LDH release observed in these samples.

4. Conclusions

In the present work, bLF was successfully modified with Ru(III) ions and the resulting LF–Ru systems were characterized using complementary experimental and computational methods. Batch sorption experiments revealed saturation-like binding behavior, with binding efficiencies ranging from 24.0 to 49.6%. Thermodynamic analysis indicated favorable and spontaneous LF–Ru formation ($\Delta G < 0$). Kinetic studies showed that most Ru(III) uptake occurred rapidly within approximately 2 min and was followed by only minor redistribution before equilibrium was reached. Fluorescence quenching confirmed strong interactions in the LF–Ru system; however, the $n \approx 1$ result should be interpreted as one dominant fluorescence-reporting binding event rather than proof that only one Ru-binding site exists in lactoferrin. Desorption experiments demonstrated only minor Ru release from LF–100Ru in SGF and SIF without enzymes, indicating high stability of this formulation under the tested conditions. At the same time, pepsin digestion showed rapid loss of the intact LF scaffold in SGF, suggesting that although Ru may remain associated with digestion fragments, receptor-mediated delivery of intact LF–Ru could be limited without additional formulation strategies. ATR-FTIR suggested loading-dependent conformational rearrangements, whereas SRCD and SAXS indicated that the overall secondary structure and solution flexibility of LF were largely preserved. Molecular docking and MD simulations identified His253 in holo-bLF as the most favorable modeled binding region and supported stable association of the $[RuCl_5]^{2-}$ species through polar and halogen-mediated contacts. DFT calculations on simplified residue models were used only as qualitative descriptors of donor preference and do not define the actual coordination environment in folded LF. TEM data further suggest that Ru-rich domains and RuO_2-like nanoparticles may arise only at the highest loading (LF–500Ru), indicating a secondary high-loading phenomenon rather than a general mechanism of LF–Ru formation. Biologically, antibacterial activity was evaluated for LF and LF–100Ru, whereas desorption was studied for LF–100Ru. Selected LF–Ru formulations produced differential cellular responses *in vitro*: LF–100Ru was relatively well tolerated by L929 fibroblasts but reduced metabolic activity in HepG2 and Caco-2 cells at 5000 mg L^{-1}, while the Caco-2 response was largely non-cytolytic according to the LDH data. Together, these results show that lactoferrin can act as an active coordination scaffold for Ru(III), but the final biological outcome depends strongly on Ru loading and on whether the system remains a protein-bound complex or proceeds to secondary Ru accumulation at high precursor concentrations.

Author contributions

The manuscript was written through contributions of all authors. T. D.-T. was responsible for the conception and design of the study, conducted the experiments, and analyzed the data; M. E. and K. R. contributed to *in vitro* experiment and corresponding data analysis; P. P. contributed to the study design and provided guidance during the research; G. T. contributed to LM, SEM-EDS, and TEM-EDS analysis and corresponding data analysis; K. S., O. P., and Ł. S. contributed to SAXS and SRCD measurements and corresponding data analysis; R. v. E. assisted in revising the manuscript; K. M., W. G., and A. K. contributed to molecular docking experiment and corresponding data analysis; R. S. and P. K. J. contributed to MD and DFT study and corresponding data analysis. T. D.-T. and P. P. drafted the manuscript and all authors participated in discussion and revision. All authors have given approval to the final version of the manuscript.

Conflicts of interest

There are no conflicts of interest to declare.

Data availability

All data supporting this study are included in the main text and the Supplementary Information (SI). The Supplementary Information file contains additional details on the isotherm and kinetic analyses of Ru(III) binding to lactoferrin, supplementary 3D fluorescence spectra, molecular modelling results from MD and DFT studies, and additional cell-imaging data related to cytotoxicity and cell viability. Supplementary Information is available. See DOI: **https://doi.org/10.1039/d6qi00255b**.

Acknowledgements

The research was financially supported in the frame of the project LIDER entitled "Development of a preparative method for the isolation of biologically active lactoferrin", project number LIDER13/0292/2022, financed by the National Centre for Research and Development (Warsaw, Poland). Tetiana Dyrda-Terniuk is a member of Emerging Fields "Cells as Experimental platforms and bioFACTories (CExFact)", and Paweł Pomastowski is a member of the Toruń Center of Excellence "Towards Personalized Medicine" operating under Excellence Initiative – Research University. We are indebted to the SAXS beamline P12 at the European Molecular Biology Laboratory (EMBL) Hamburg, located at the PETRA III storage ring, and we acknowledge the use of the CD beamline at ASTRID2, Department of Physics and Astronomy, Aarhus University, Denmark.

References

1 S. Jeyaraj, The role of transition metals in biological systems, *Biochem. Physiol.*, 2023, **12**, 441.

2 G. Ferraro and A. Merlino, Investigation of metallodrug/protein interaction by X-ray crystallography and complementary biophysical techniques, *Inorg. Chem. Front.*, 2025, **12**, 3345–3366.

3 Y. J. Liu, Z. H. Liang, X. L. Hong, Z. Z. Li, J. H. Yao and H. L. Huang, Synthesis, characterization, cytotoxicity, apoptotic inducing activity, cellular uptake, interaction of DNA binding and antioxidant activity studies of ruthenium(II) complexes, *Inorg. Chim. Acta*, 2012, **387**, 117–124.

4 F. Li, J. G. Collins and F. R. Keene, Ruthenium complexes as antimicrobial agents, *Chem. Soc. Rev.*, 2015, **44**, 2529–2542.

5 K. M. Mahmud, M. S. Niloy, M. S. Shakil and M. A. Islam, Ruthenium complexes: an alternative to platinum drugs in colorectal cancer treatment, *Pharmaceutics*, 2021, **13**, 1295.

6 M. Małecka, A. Skoczyńska, D. M. Goodman, C. G. Hartinger and E. Budzisz, Biological properties of ruthenium(II)/(III) complexes with flavonoids as ligands, *Coord. Chem. Rev.*, 2021, **436**, 213849.

7 M. Richert, G. Trykowski, M. Walczyk, M. J. Cieślak, J. Kaźmierczak-Barańska, K. Królewska-Golińska, J. W. Sobczak and S. Biniak, Modification of multiwalled carbon nanotubes with a ruthenium drug candidate - indazolium[tetrachlorobis(1H-indazole)ruthenate(III)] (KP1019), *Dalton Trans.*, 2020, **49**, 16791–16800.

8 K. Lin, Z. Z. Zhao, H. B. Bo, X. J. Hao and J. Q. Wang, Applications of ruthenium complex in tumor diagnosis and therapy, *Front. Pharmacol.*, 2018, **9**, 1323.

9 S. Katheria, Ruthenium complexes as potential cancer cell growth inhibitors for targeted chemotherapy, *ChemistrySelect*, 2022, **7**, e202201645.

10 T. Dyrda-Terniuk and P. Pomastowski, The multifaceted roles of bovine lactoferrin: molecular structure, isolation methods, analytical characteristics, and biological properties, *J. Agric. Food Chem.*, 2023, **71**, 20500–20531.

11 T. Uchida, T. Suguri and S. Harjinder, Folic acid and/or vitamin B12-lactoferrin complex, *US Pat*, 6500472B2, 2002.

12 Z. Q. Ming, H. Li, H. Sun and K. Ho, Targeted drug delivery via the transferrin receptor-mediated endocytosis pathway, *Phatrmacol. Rev.*, 2002, **54**, 561–587.

13 L. Rosa, A. Cutone, M. S. Lepanto, M. J. Scotti, M. P. Conte, R. Paesano and P. Valenti, Physico-chemical properties influence the functions and efficacy of commercial bovine lactoferrins, *BioMetals*, 2018, **31**, 301–312.

14 J. R. Kanwar, G. Mahidhara and R. K. Kanwar, Novel alginate-enclosed chitosan-calcium phosphate-loaded iron-saturated bovine lactoferrin nanocarriers for oral delivery in colon cancer therapy, *Nanomedicine*, 2012, **7**, 1521–1550.

15 D. B. Kell, E. L. Heyden and E. Pretorius, The biology of lactoferrin, an iron-binding protein that can help defend against viruses and bacteria, *Front. Immunol.*, 2020, **11**, 1221.

16 A. K. Kondapi, Targeting cancer with lactoferrin nanoparticles: recent advances, *Nanomedicine*, 2020, **15**, 2071–2083.

17 A. L. Arsene, V. Uivarosi, N. Mitrea, C. M. Dragoi and A. Nicolae, The binding properties of some novel ruthenium(III) complexes with human serum transferrin, *Biopolym. Cell*, 2011, **27**, 141–146.

18 M. Pongratz, P. Schluga, M. A. Jakupec, V. B. Arion, C. G. Hartinger, G. Allmaier and B. K. Keppler, Transferrin binding and transferrin-mediated cellular uptake of the ruthenium coordination compound KP1019, studied by means of AAS, ESI-MS and CD spectroscopy, *J. Anal. At. Spectrom.*, 2004, **19**, 46–51.

19 A. Levina, A. R. M. Chetcuti and P. A. Lay, Controversial role of transferrin in the transport of ruthenium anticancer drugs, *Biomolecules*, 2022, **12**, 1319.

20 M. Wang, H. Wang, X. Xu, T. P. Lai, Y. Zhou, Q. Hao, H. Li and H. Sun, Binding of ruthenium and osmium at non-iron sites of transferrin accounts for their iron-independent cellular uptake, *J. Inorg. Biochem.*, 2022, **234**, 111885.

21 S. J. Kim, D. Y. Yu, K. W. Pak, S. Jeong, S. W. Kim and K. K. Lee, Structure of the human lactoferrin gene and its chromosomal localization, *Mol. Cells*, 1998, **8**, 663–668.

22 T. D. Y. Chung and K. N. Raymond, Lactoferrin: The role of conformational changes in its iron binding and release, *J. Am. Chem. Soc.*, 1993, **115**, 6765–6768.

23 H. Li and Z. M. Qian, Transferrin/transferrin receptor-mediated drug delivery, *Med. Res. Rev.*, 2002, **22**, 225–250.

24 E. N. Baker and H. M. Baker, A structural framework for understanding the multifunctional character of lactoferrin, *Biochimie*, 2009, **91**, 3–10.

25 Z. S. Abbas, Z. N. Nasif and A. T. Tawfeeq, Overview of drug-loaded lactoferrin nanoparticles in lung cancer therapy, *Next Nanotechnol.*, 2025, **8**, 100302.

26 A. Lebedeva, B. L. Albuquerque, J. B. Domingos, J. F. Lamonier, J. M. Giraudon, P. Lecante, A. Denicourt-Nowicki and A. Roucoux, Ruthenium trichloride catalyst in water: Ru colloids versus Ru dimer characterization investigations, *Inorg. Chem.*, 2019, **58**, 4141–4151.

27 S. K. Shukla, The study of ruthenium(III) complexes by paper electrophoresis and spectrophotometry: Solution chemistry of potassium aquopentachlororuthenite. Effect of ageing, *J. Chromatogr. A*, 1962, **8**, 96–102.

28 M. M. T. Khan, G. Ramachandraiah and R. S. Shukla, Ruthenium(III) chloride in aqueous solution: Effects of temperature, ionic strength and solvent isotope on aquation and anation reactions of the chloro complexes, *Polyhedron*, 1992, **11**, 3075–3081.

29 T. Dyrda-Terniuk and P. Pomastowski, Impact of ultrafiltration on the physicochemical properties of bovine lactoferrin: insights into molecular mass, surface morphology, and elemental composition, *J. Dairy Sci.*, 2024, **107**, 10280–10298.

30 A. Micsonai, E. Moussong, F. Wien, E. Boros, H. Vadaszi, N. Murvai, Y.-H. Lee, T. Molnar, M. Refregiers, Y. Goto, A. Tantos and J. Kardos, BeStSel: webserver for secondary structure and fold prediction for protein CD spectroscopy, *Nucleic Acids Res.*, 2022, **50**, W90–W98.

31 C. E. Blanchet, A. Spilotros, F. Schwemmer, M. A. Graewert, A. Kikhney, C. M. Jeffries, D. Franke, D. Mark, R. Zengerle, F. Cipriani, S. Fiedler, M. Roessle and D. I. Svergun, Versatile sample environments and automation for biological solution X-Ray scattering experiments at the P12 beamline (PETRA III, DESY), *J. Appl. Crystallogr.*, 2015, **48**, 431–443.

32 K. Manalastas-Cantos, P. V. Konarev, N. R. Hajizadeh, A. G. Kikhney, M. V. Petoukhov, D. S. Molodenskiy, A. Panjkovich, H. D. T. Mertens, A. Gruzinov, C. Borges, C. M. Jeffries, D. I. Sverguna and D. Frankea, ATSAS 3.0: expanded functionality and new tools for small-angle scattering data analysis, *J. Appl. Crystallogr.*, 2021, **54**, 343–355.

33 D. Franke and D. I. Svergun, DAMMIF, a program for rapid *ab initio* shape determination in small-angle scattering, *J. Appl. Crystallogr.*, 2009, **42**, 342–346.

34 D. Franke, M. V. Petoukhov, P. V. Konarev, A. Panjkovich, A. Tuukkanen, H. D. T. Mertens, A. G. Kikhney, N. R. Hajizadeh, J. M. Franklin, C. M. Jeffries and D. I. Svergun, ATSAS 2.8: a comprehensive data analysis suite for small-angle scattering from macromolecular solutions, *J. Appl. Crystallogr.*, 2017, **50**, 1212–1225.

35 D. I. Svergun, Determination of the regularization parameter in indirect-transform methods using perceptual criteria, *J. Appl. Crystallogr.*, 1992, **25**, 495–503.

36 European Directorate for the Quality of Medicines & HealthCare (EDQM), *European Pharmacopoeia*, Council of Europe, Strasbourg, 7th edn, 2011.

37 O. Pryshchepa, P. Pomastowski, K. Rafińska, A. Gołębiowski, A. Rogowska, M. Monedeiro-Milanowski, G. Sagandykova, B. Michalke, P. Schmitt-Kopplin, M. Gloc, R. Dobrucka, K. Kurzydłowski and B. Buszewski, Synthesis, physicochemical characterization, and antibacterial performance of silver–lactoferrin complexes, *Int. J. Mol. Sci.*, 2022, **23**, 7112.

38 S. A. Moore, B. F. Anderson, C. R. Groom, M. Haridas and E. N. Baker, Three-dimensional structure of diferric bovine lactoferrin at 2.8 Å resolution, *J. Mol. Biol.*, 1997, **274**, 222–236.

39 N. Rastogi, A. Singh, S. N. Pandey, M. Sinha, A. Bhushan, P. Kaur, S. Sharma and T. P. Singh, Structure of the iron-free true C-terminal half of bovine lactoferrin produced by tryptic digestion and its functional significance in the gut, *FEBS J.*, 2014, **281**, 2871–2882.

40 G. Madhavi Sastry, M. Adzhigirey, T. Day, R. Annabhimoju and W. Sherman, Protein and ligand preparation: parameters, protocols, and influence on virtual screening enrichments, *J. Comput.-Aided Mol. Des.*, 2013, **27**, 221–234.

41 C. R. Søndergaard, M. H. M. Olsson, M. Rostkowski and J. H. Jensen, Improved treatment of ligands and coupling effects in empirical calculation and rationalization of pKa values, *J. Chem. Theory Comput.*, 2011, **7**, 2284–2295.

42 C. Lu, C. Wu, D. Ghoreishi, W. Chen, L. Wang, W. Damm, G. A. Ross, M. K. Dahlgren, E. Russell, C. D. Von Bargen, R. Abel, R. A. Friesner and E. D. Harder, OPLS4: improving force field accuracy on challenging regimes of chemical space, *J. Chem. Theory Comput.*, 2021, **17**, 4291–4300.

43 A. D. Bochevarov, E. Harder, T. F. Hughes, J. R. Greenwood, D. A. Braden, D. M. Philipp, D. Rinaldo, M. D. Halls, J. Zhang and R. A. Friesner, Jaguar: A high-performance quantum chemistry software program with strengths in life and materials sciences, *Int. J. Quantum Chem.*, 2013, **113**, 2110–2142.

44 M. L. A. Hakkennes, F. Buda and S. Bonnet, MetalDock: an open access docking tool for easy and reproducible docking of metal complexes, *J. Chem. Inf. Model.*, 2023, **63**, 7816–7825.

45 R. A. Friesner, J. L. Banks, R. B. Murphy, T. A. Halgren, J. J. Klicic, D. T. Mainz, M. P. Repasky, E. H. Knoll, M. Shelley, J. K. Perry, D. E. Shaw, P. Francis and P. S. Shenkin, Glide: a new approach for rapid, accurate docking and scoring. 1. method and assessment of docking accuracy, *J. Med. Chem.*, 2004, **47**, 1739–1749.

46 W. Sherman, T. Day, M. P. Jacobson, R. A. Friesner and R. Farid, Novel procedure for modeling ligand/receptor induced fit effects, *J. Med. Chem.*, 2006, **49**, 534–553.

47 M. J. Frisch, G. W. Trucks, H. B. Schlegel, G. E. Scuseria, M. A. Robb, J. R. Cheeseman, G. Scalmani, V. Barone, G. A. Petersson, H. Nakatsuji, *et al.*, *Gaussian 16, Revision C.01*, Gaussian, Inc., Wallingford, CT, 2016.

48 S. Demir and M. F. Fellah, A DFT study on Pt doped (4,0) SWCNT: CO adsorption and sensing, *Appl. Surf. Sci.*, 2020, **504**, 144141.

49 G. Gecim, M. Ozekmekci and M. F. Fellah, Ga and Ge-doped graphene structures: a DFT study of sensor applications for methanol, *Comput. Theor. Chem.*, 2020, **1180**, 112828.

50 H. J. C. Berendsen, D. van der Spoel and R. van Drunen, GROMACS: a message-passing parallel molecular dynamics implementation, *Comput. Phys. Commun.*, 1995, **91**, 43–56.

51 A. D. Mackerell, N. Banavali and N. Foloppe, Development and current status of the CHARMM force field for nucleic acids, *Biopolymers*, 2001, **56**, 257–265.

52 A. M. A. Abdelgawwad and A. Francés-Monerris, EasyPARM: automated, versatile, and reliable force field parameters for metal-containing molecules with unique labeling of coordinating atoms, *J. Chem. Theory Comput.*, 2025, **21**, 1817–1830.

53 P. Mark and L. Nilsson, Structure and dynamics of the TIP3P, SPC, and SPC/E water models at 298 K, *J. Phys. Chem. A*, 2001, **105**, 9954–9960.

54 B. Abebe, H. C. A. Murthy and E. Amare, Summary on adsorption and photocatalysis for pollutant remediation: mini review, *J. Encapsulation Adsorpt. Sci.*, 2018, **8**, 225–255.

55 O. Pryshchepa, K. Rafińska, A. Gołębiowski, M. Sugajski, G. Sagandykova, P. Madajski, B. Buszewski and P. Pomastowski, Synthesis and physicochemical characterization of bovine lactoferrin supersaturated complex with iron(III) ions, *Sci. Rep.*, 2022, **12**, 12695.

56 R. Jabbari and N. Ghasemi, Evaluating the efficiency of two-parameter adsorption isotherm models in the adsorption of methylene blue, *Iran. J. Chem. Chem. Eng.*, 2024, **43**, 1533–1549.

57 I. M. Raimondi, V. G. S. Rodrigues, J. Z. Lima, J. P. Marques and L. A. A. Vaz, The potential use of press-mud as reactive material for Cd2+ removal: adsorption equilibrium, kinetics, desorption, and bioaccessibility, *Water, Air, Soil Pollut.*, 2020, **231**, 365.

58 S. Suresh, V. C. Srivastava and I. M. Mishra, Adsorption of hydroquinone in aqueous solution by granulated activated carbon, *J. Environ. Eng.*, 2011, **137**, 1145–1157.

59 X. Chen, J. C. Fan, Y. Wang, C. P. Fan and Z. C. Shang, Fluorometric study on the interaction between lomefloxacin and bovine lactoferrin, *Anal. Sci.*, 2006, **22**, 427–430.

60 O. Mazuryk, K. Kurpiewska, K. Lewiński, G. Stochel and M. Brindell, Interaction of apo-transferrin with anticancer ruthenium complexes NAMI-A and its reduced form, *J. Inorg. Biochem.*, 2012, **116**, 11–18.

61 S. G. Stevenson and K. R. Preston, Intrinsic Fluorescence and Quenching Studies of Gluten Proteins, *Cereal Chem.*, 1994, **71**, 155–159.

62 Y. Lu, D. Zhu, L. Gui, Y. Li, W. Wang, J. Liu and Y. Wang, A dual-targeting ruthenium nanodrug that inhibits primary tumor growth and lung metastasis via the PARP/ATM pathway, *J. Nanobiotechnol.*, 2021, **19**, 115.

63 S. H. Razavizadegan Jahromi, R. Farhoosh, B. Hemmateenejad and M. Varidi, Characterization of the binding of cyanidin-3-glucoside to bovine serum albumin and its stability in a beverage model system: a multispectroscopic and chemometrics study, *Food Chem.*, 2020, **311**, 126015.

64 J. Keizer, Nonlinear fluorescence quenching and the origin of positive curvature in Stern-Volmer plots, *J. Am. Chem. Soc.*, 1983, **105**, 1494–1498.

65 E. Ciotta, P. Prosposito and R. Pizzoferrato, Positive curvature in Stern-Volmer plot described by a generalized model for static quenching, *J. Lumin.*, 2019, **206**, 518–522.

66 M. Maruthamuthu and G. Selvakumar, Selective quenching of tryptophanyl fluorescence in bovine serum albumin by the iodide ion, *Proc. – Indian Acad. Sci., Chem. Sci.*, 1995, **107**, 79–86.

67 J. M. Steijns and A. C. M. Van Hooijdonk, Occurrence, structure, biochemical properties and technological characteristics of lactoferri, *Br. J. Nutr.*, 2000, **84**, S11–S17.

68 C. Wang, Y. Lu, B. Xia, X. Li, X. Huang and C. Dong, Complexation of bovine lactoferrin with selected phenolic acids via noncovalent interactions: binding mechanism and altered functionality, *J. Dairy Sci.*, 2024, **107**, 4189–4204.

69 M. Yan, Y. Wang, X. Shen, S. Dong, M. Diao, Y. Zhao and T. Zhang, Enhanced foaming properties of lactoferrin by forming functional complexes with ginsenoside Re and Rb1, *Food Hydrocolloids*, 2022, **123**, 107159.

70 F. C. Santos, P. J. Costa, M. H. Garcia and T. S. Morais, Binding of RuCp complexes with human apo-transferrin: fluorescence spectroscopy and molecular docking methods, *BioMetals*, 2021, **34**, 1029–1042.

71 O. Pryshchepa, G. Sagandykova, J. Rudnicka, P. Pomastowski, M. Sprynskyy and B. Buszewski, Synthesis and physicochemical characterization of zinc-lactoferrin complexes, *J. Dairy Sci.*, 2022, **105**, 1940–1958.

72 H. Bokkhim, N. Bansal, L. Grøndahl and B. Bhandari, Interactions between different forms of bovine lactoferrin and sodium alginate affect the properties of their mixtures, *Food Hydrocolloids*, 2015, **48**, 38–46.

73 Y. He, Y. Lu, Y. Liu, R. Zhao, B. Xia, Y. Zhang, X. Huang and C. Wang, Fabrication and characterisation of stable ternary complexes based on bovine lactoferrin, pectin and chlorogenic acid, *Int. J. Dairy Technol.*, 2024, **77**, 1097–1108.

74 N. Paseban, P. Ghadam and P. S. Pourhosseini, The fluorescence behavior and stability of AgNPs synthesized by juglans regia green husk aqueous extract, *Int. J. Nanosci. Nanotechnol.*, 2019, **15**, 117–126.

75 H. Bokkhim, N. Bansal, L. Grøndahl and B. Bhandari, Physico-chemical properties of different forms of bovine lactoferrin, *Food Chem.*, 2013, **141**, 3007–3013.

76 C. Guo, X. Guo, W. Chu, N. Jiang and H. Li, Spectroscopic study of conformation changes of bovine serum albumin in aqueous environment, *Chin. Chem. Lett.*, 2019, **30**, 1302–1306.

77 S. P. Valappil, E. A. Abou Neel, K. M. Zakir Hossain, W. Paul, D. Cherukaraveedu, B. Wade, T. I. Ansari, C. K. Hope, S. M. Higham and C. P. Sharma, Novel lactoferrin-conjugated gallium complex to treat Pseudomonas aeruginosa wound infection, *Int. J. Biol. Macromol.*, 2024, **258**, 128838.

78 N. Igci and F. D. Ozel Demiralp, A Fourier transform infrared spectroscopic investigation of Macrovipera lebetina lebetina and M. l. Obtusa crude venoms, *Eur. J. Biol.*, 2020, **79**, 14–22.

79 E. Vanea, K. Magyari and V. Simon, Protein attachment on aluminosilicates surface studied by XPS and FTIR spectroscopy, *J. Optoelectron. Adv. Mater.*, 2010, **12**, 1206–1212.

80 A. Barth, Infrared spectroscopy of proteins, *Biochim. Biophys. Acta, Bioenerg.*, 2007, **1767**, 1073–1101.

81 D. Usoltsev, V. Sitnikova, A. Kajava and M. Uspenskaya, Systematic FTIR spectroscopy study of the secondary structure changes in human serum albumin under various denaturation conditions, *Biomolecules*, 2019, **9**, 359.

82 S. Chen, T. Zhao, W. Jiao, Y. Zhang, W. Liu, Y. Zhang, L. Huang and S. Lv, Inhibited digestion of lactoferrin -

lactose complexes: preparation, structural characterization and digestion behaviors, *LWT*, 2022, **172**, 114141.

83 H. A. Alhazmi, M. Al Bratty, A. M. Meraya, A. Najmi, M. S. Alam, S. A. Javed and W. Ahsan, Spectroscopic characterization of the interactions of bovine serum albumin with medicinally important metal ions: platinum (IV), iridium(III) and iron(II), *Acta Biochim. Pol.*, 2021, **68**, 99–107.

84 G. Wang, Y. Lu and Y. Liu, Probing the binding behavior and kinetics of silver nanoparticles with bovine serum albumin, *RSC Adv.*, 2017, **7**, 9393–9401.

85 J. M. Hadden, M. Bloemendal, P. I. Haris, S. K. S. Srai and D. Chapman, Fourier transform infrared spectroscopy and differential scanning calorimetry of transferrins: human serum transferrin, rabbit serum transferrin and human lactoferrin, *Biochim. Biophys. Acta*, 1994, **1205**, 59–67.

86 M. Kaur, S. Singh and A. Kaur, Structural changes in Amide I and Amide II regions of PCOS women analyzed by ATR-FTIR spectroscopy, *Heliyon*, 2024, **10**, e33494.

87 J. L. R. Arrondo and F. M. Goñi, Structure and dynamics of membrane proteins as studied by infrared spectroscopy, *Prog. Biophys. Mol. Biol.*, 1999, **72**, 367–405.

88 Y. Yang, G. Greco, D. Maniglio, B. Mazzolai, C. Migliaresi, N. Pugno and A. Motta, Spider (Linothele megatheloides) and silkworm (Bombyx mori) silks: comparative physical and biological evaluation, *Mater. Sci. Eng., C*, 2020, **107**, 110197.

89 G. Duca, L. Anghel and R. V. Erhan, Structural aspects of lactoferrin and serum transferrin observed by FTIR spectroscopy, *Chem. J. Mold.*, 2018, **13**, 111–116.

90 S. Karthikeyan, FTIR and ICP-AES study of the effect of heavy metals nickel and chromium in tissue protein of an edible fish Cirrhinus mrigala, *Rom. J. Biophys.*, 2012, **22**, 95–105.

91 B. R. Singh, D. B. DeOliveira, F.-N. Fu and M. P. Fuller, Fourier transform infrared analysis of Amide III bands of proteins for the secondary structure estimation, in *Biomol. Spectrosc. III*, 1993, vol. 1890, pp. 47–55.

92 C. Stani, L. Vaccari, E. Mitri and G. Birarda, FTIR investigation of the secondary structure of type I collagen: new insight into the Amide III band, *Spectrochim. Acta, Part A*, 2020, **229**, 118006.

93 L. Voronina, F. Fleischmann, J. Šimunović, C. Ludwig, M. Novokmet and M. Žigman, Probing blood plasma protein glycosylation with infrared spectroscopy, *Anal. Chem.*, 2023, **96**, 2830–2839.

94 A. Derenne, K. M. Derfoufi, B. Cowper, C. Delporte and E. Goormaghtigh, FTIR spectroscopy as an analytical tool to compare glycosylation in therapeutic monoclonal antibodies, *Anal. Chim. Acta*, 2020, **1112**, 62–71.

95 A. M. Marques, A. I. Bourbon, R. M. Rodrigues, J. A. Teixeira, L. M. Pastrana and M. A. Cerqueira, Lactoferrin as a carrier of iron: development and physicochemical characterization, *Food Hydrocolloids*, 2023, **142**, 108772.

96 R. Pribic, I. H. M. van Stokkum, D. Chapman, P. I. Haris and M. Bloemendal, Protein secondary structure from Fourier transform infrared and/or circular dichroism spectra, *Anal. Biochem.*, 1993, **214**, 366–378.

97 J. C. Gorga, A. Dong, M. C. Manning, R. W. Woody, W. S. Caughey and J. L. Strominger, Comparison of the secondary structures of human class I and class II major histocompatibility complex antigens by Fourier transform infrared and circular dichroism spectroscopy, *Proc. Natl. Acad. Sci. U. S. A.*, 1989, **86**, 2321–2325.

98 H. Rosenkranz, Circular dichroism of globular proteins: a review of the limits of the CD methods for the calculation of secondary structure, *Clin. Chem. Lab. Med.*, 1974, **12**, 415–424.

99 W. C. Johnson, Analyzing protein circular dichroism spectra for accurate secondary structures, *Proteins: Struct., Funct., Genet.*, 1999, **35**, 307–312.

100 Y. Huang, Y. Tao, H. Yang, J. Zhang, B. Yan, H. Zhang, W. Chen and D. Fan, Critical importance of iron saturation in lactoferrin: effects on biological activity, nutritional functions, and applications, *J. Agric. Food Chem.*, 2025, **73**, 10665–10680.

101 Y. Lee, C. Scheurer and K. Reuter, Epitaxial core-shell oxide nanoparticles: first-principles evidence for increased activity and stability of rutile catalysts for acidic oxygen evolution, *ChemSusChem*, 2022, **15**, e202200015.

102 S. B. He, P. Balasubramanian, Z. W. Chen, Q. Zhang, Q. Q. Zhuang, H. P. Peng, H. H. Deng, X. H. Xia and W. Chen, Protein-supported RuO2 nanoparticles with improved catalytic activity, in vitro salt resistance, and biocompatibility: colorimetric and electrochemical biosensing of cellular H_2O_2, *ACS Appl. Mater. Interfaces*, 2020, **12**, 14876–14883.

103 H. Ilyas, S. Tomar, S. K. Miglani and D. S. Raghav, Environmentally friendly approach to ruthenium oxide (RuO2) nanoparticle synthesis: a dual study of antimicrobial effectiveness and magnetic properties, *Next Nanotechnol.*, 2025, **8**, 100217.

104 S. Kaur, N. K. Bari and S. Sinha, Varying protein architectures in 3-dimensions for scaffolding and modulating properties of catalytic gold nanoparticles, *Amino Acids*, 2022, **54**, 441–454.

105 A. Imtiyaz and A. Singh, Green synthesis of ruthenium oxide nanoparticles mediated extract of Ephedra gerandiana for their photocatalytic and biological activities, *Next Mater.*, 2025, **9**, 101214.

106 G. Majka, K. Śpiewak, K. Kurpiewska, P. Heczko, G. Stochel, M. Strus and M. Brindell, A high-throughput method for the quantification of iron saturation in lactoferrin preparations, *Anal. Bioanal. Chem.*, 2013, **405**, 5191–5200.

107 S. F. Hansen, S. D. Nielsen, J. T. Rasmusen, L. B. Larsen and L. Wiking, Disulfide bond formation is not crucial for the heat-induced interaction between β-lactoglobulin and milk fat globule membrane proteins, *J. Dairy Sci.*, 2020, **103**, 5874–5881.

108 M. E. Caetano-Silva, F. M. Netto, M. T. Bertoldo-Pacheco, A. Alegría and A. Cilla, Peptide-metal complexes: obten-

tion and role in increasing bioavailability and decreasing the pro-oxidant effect of minerals, *Crit. Rev. Food Sci. Nutr.*, 2021, **61**, 1470–1489.

109 L. Zhang, Y. Chen and S. Bonnet, Ruthenium complexes in protein science: heading a new generation of therapeutic and analytical tools, *Angew. Chem., Int. Ed.*, 2026, **65**, e14884.

110 M. Martinez-Alonso and G. Gasser, Ruthenium polypyridyl complex-containing bioconjugates, *Coord. Chem. Rev.*, 2021, **434**, 213736.

111 H. M. Baker and E. N. Baker, Lactoferrin and Iron: structural and dynamic aspects of binding and release, *BioMetals*, 2004, **17**, 209–216.

112 E. Kilic, M. V. Novoselova, S. H. Lim, N. A. Pyataev, S. I. Pinyaev, O. A. Kulikov, O. A. Sindeeva, O. A. Mayorova, R. Murney, M. N. Antipina, B. Haigh, G. B. Sukhorukov and M. V. Kiryukhin, Formulation for oral delivery of lactoferrin based on bovine serum albumin and tannic acid multilayer microcapsules, *Sci. Rep.*, 2017, **7**, 44159.

113 Z. Niu, S. M. Loveday, V. Barbe, I. Thielen, Y. He and H. Singh, Protection of native lactoferrin under gastric conditions through complexation with pectin and chitosan, *Food Hydrocolloids*, 2019, **93**, 120–130.

114 V. A. Emel'yanov, A. V. Virovets and I. A. Baidina, Crystal structure of ammonium pentachloroaquaruthenate(III) (NH4)2[Ru(H_2O)Cl5], *J. Struct. Chem.*, 2008, **49**, 566–569.

115 E. N. Biernbaum, A. Gnezda, S. Akbar, R. Franklin, P. A. Venturelli and J. L. McKillip, Lactoferrin as an antimicrobial against Salmonella enterica and Escherichia coli O157:H7 in raw milk, *JDS Commun.*, 2021, **2**, 92–97.

116 D. A. Dionysius, P. A. Grieve and J. M. Milne, Forms of lactoferrin: their antibacterial effect on enterotoxigenic Escherichia coli, *J. Dairy Sci.*, 1993, **76**, 2597–2606.

117 H. Saito, H. Miyakawa, N. Ishibashi, Y. Tamura, H. Hayasawa and S. Shimamura, Effect of iron-free and metal-bound forms of lactoferrin on the growth of Bifidobacteria, *E. coli* and S. aureus, *Biosci. Microflora*, 1996, **15**, 1–7.

118 G. Majka, M. Pilarczyk-Zurek, A. Baranowska, B. Skowron and M. Strus, actoferrin metal saturation—which form is the best for neonatal nutrition?, *Nutrients*, 2020, **12**, 3340.

119 A. Del Olmo, J. Calzada and M. Nuñez, Effect of lactoferrin and its derivatives against Gram-positive bacteria in vitro and, combined with high pressure, in chicken breast fillets, *Meat Sci.*, 2012, **90**, 71–76.

120 J. Garbe, J. Sjögren, E. F. J. Cosgrave, W. B. Struwe, M. Bober, A. I. Olin, P. M. Rudd and M. Collin, EndoE from Enterococcus faecalis hydrolyzes the glycans of the biofilm inhibiting protein lactoferrin and mediates growth, *PLoS One*, 2014, **9**, e91035.

121 M. Monedeiro-Milanowski, F. Monedeiro and P. Pomastowski, Silver lactoferrin as antimicrobials: mechanisms of action and resistance assessed by bacterial molecular profiles, *ACS Omega*, 2023, **8**, 46236–46251.

122 P. Pomastowski, M. Sprynskyy, P. Žuvela, K. Rafińska, M. Milanowski, J. J. Liu, M. Yi and B. Buszewski, Silver-lactoferrin nanocomplexes as a potent antimicrobial agent, *J. Am. Chem. Soc.*, 2016, **138**, 7899–7909.

123 F. Li, J. G. Collins and F. R. Keene, Ruthenium complexes as antimicrobial agents, *Chem. Soc. Rev.*, 2015, **44**, 2529–2542.

124 M. Murata, H. Wakabayashi, K. Yamauchi and F. Abe, Identification of milk proteins enhancing the antimicrobial activity of lactoferrin and lactoferricin, *J. Dairy Sci.*, 2013, **96**, 4891–4898.

125 T. Kutila, S. Pyörälä, H. Saloniemi and L. Kaartinen, Antibacterial effect of bovine lactoferrin against udder pathogens, *Acta Vet. Scand.*, 2003, **44**, 35–42.

126 R. Jing, Q. L. Yi, C. Zhuo, W. Kang, Q. W. Yang, Y. S. Yu, B. Zheng, Y. Li, F. P. Hu, Y. Yang, J. Lin, G. Zhang, J. J. Zhang, T. Wang, J. Li, C. Y. Zhuo, X. Li, Y. F. Zhu and Y. C. Xu, Establishment of epidemiological cut-off values for eravacycline, against Escherichia coli, Klebsiella pneumoniae, Enterobacter cloacae, Acinetobacter baumannii and Staphylococcus aureus, *J. Antimicrob. Chemother.*, 2024, **79**, 2246–2250.

127 B. Çetinkaya, E. Çetinkaya, H. Kucukbay and R. Durmaz, Antimicrobial activity of carbene complexes of Rhodium(I) and Ruthenium(II), *Arzneim.-Forsch./Drug Res.*, 1996, **46**, 821–823.

128 M. Sinha, S. Kaushik, P. Kaur, S. Sharma and T. P. Singh, Antimicrobial lactoferrin peptides: the hidden players in the protective function of a multifunctional protein, *Int. J. Pept.*, 2013, **2013**, 390230.

129 S. Farnaud, A. Patel, E. W. Odell and R. W. Evans, Variation in antimicrobial activity of lactoferricin-derived peptides explained by structure modelling, *FEMS Microbiol. Lett.*, 2004, **238**, 221–226.

130 M. Tomita, W. Bellamy, M. Takase, K. Yamauchi, H. Wakabayashi and K. Kawase, Potent antibacterial peptides generated by pepsin digestion of bovine lactoferrin, *J. Dairy Sci.*, 1991, **74**, 4137–4142.

131 H. Saito, H. Miyakawa, Y. Tamura, S. Shimamura and M. Tomita, Potent bactericidal activity of bovine lactoferrin hydrolysate produced by heat treatment at acidic pH, *J. Dairy Sci.*, 1991, **74**, 3724–3730.

132 K. Yamauchi, M. Tomita, T. J. Giehl and R. T. Ellison, Antibacterial activity of lactoferrin and a pepsin-derived lactoferrin peptide fragment, *Infect. Immun.*, 1993, **61**, 719–728.

133 T. Matsuzaki, M. Nakamura, T. Nogita and A. Sato, Cellular uptake and release of intact lactoferrin and its derivatives in an intestinal enterocyte model of Caco-2 cells, *Biol. Pharm. Bull.*, 2019, **42**, 989–995.

134 X. Zhao, X. X. Xu, Y. Liu, E. Z. Xi, J. J. An, D. Tabys and N. Liu, The in vitro protective role of bovine lactoferrin on intestinal epithelial barrier, *Molecules*, 2019, **24**, 148.

135 S. Kapitza, M. Pongratz, M. A. Jakupec, P. Heffeter, W. Berger, L. Lackinger, B. K. Keppler and B. Marian, Heterocyclic complexes of ruthenium(III) induce apoptosis

in colorectal carcinoma cells, *J. Cancer Res. Clin. Oncol.*, 2005, **131**, 101–110.

136 C. C. Zeng, S. H. Lai, J. H. Yao, C. Zhang, H. Yin, W. Li, B. J. Han and Y. J. Liu, The induction of apoptosis in HepG-2 cells by ruthenium(II) complexes through an intrinsic ROS-mediated mitochondrial dysfunction pathway, *Eur. J. Med. Chem.*, 2016, **122**, 118–126.

137 M. Cocchietto, S. Zorzet and G. Sava, Synthesis and chemical-pharmacological characterization of the antimetastatic NAMI-A-type Ru(III) complexes (Hdmtp)[trans-RuCl 4 (dmso-S)(dmtp)], (Na)[trans-RuCl4(dmso-S)(dmtp)], and 5,7-dimethyl[1,2,4]triazolo[1,5-a]pyrimidine), *J. Med. Chem.*, 2004, **47**, 1110–1121.

138 M. Groessl, E. Reisner, C. G. Hartinger, R. Eichinger, O. Semenova, A. R. Timerbaev, M. a. Jakupec, V. B. Arion and B. K. Keppler, Structure–activity relationships for NAMI-A-type complexes (HL)[trans-RuCl4L(S-dmso)ruthenate(III)] (L = imidazole, indazole, 1,2,4-triazole, 4-amino-1,2,4-triazole, and 1-methyl-1,2,4-triazole): aquation, redox properties, protein binding, and antiproliferative activity, *J. Med. Chem.*, 2007, **50**, 2185–2193.